

FRONT MATTER

Title: Wearable microneedle-based electrochemical aptamer biosensing for precision dosing of drugs with narrow therapeutic windows

Authors

Shuyu Lin^{1,2,†}, Xuanbing Cheng^{1,2,3,†}, Jialun Zhu^{1,2,3,†}, Bo Wang^{1,2}, David Jelinek^{4,5}, Yichao Zhao^{1,2,3}, Tsung-Yu Wu^{1,2,3}, Abraham Horrillo⁴, Jiawei Tan^{1,2,3}, Justin Yeung^{1,3}, Wenzhong Yan⁷, Sarah Forman^{1,4}, Hilary A. Coller^{4,6,8}, Carlos Milla⁹, Sam Emaminejad^{1,2,10*}

Affiliations

¹Interconnected & Integrated Bioelectronics Lab (I²BEL), University of California, Los Angeles.

²Department of Electrical and Computer Engineering, University of California, Los Angeles.

³Department of Materials Science and Engineering, University of California, Los Angeles.

⁴Department of Molecular, Cell and Developmental Biology, University of California, Los Angeles.

⁵Weintraub Center for Reconstructive Biotechnology, School of Dentistry, University of California, Los Angeles.

⁶Department of Biological Chemistry, David Geffen School of Medicine, University of California, Los Angeles.

⁷Department of Mechanical and Aerospace Engineering, University of California, Los Angeles.

⁸Molecular Biology Institute, University of California, Los Angeles.

⁹The Stanford Cystic Fibrosis Center, Center for Excellence in Pulmonary Biology, Stanford School of Medicine.

¹⁰Department of Bioengineering, University of California, Los Angeles.

†These authors contributed equally to this work.

*Corresponding author. Email: emaminejad@ucla.edu

Abstract

Therapeutic drug monitoring is essential for dosing pharmaceuticals with narrow therapeutic windows. Nevertheless, standard methods are imprecise and involve invasive/resource-intensive procedures with long turnaround times. Overcoming these limitations, we present a microneedle-based electrochemical aptamer biosensing patch (μ NEAB-patch) that minimally-invasively probes the interstitial fluid (ISF) and renders correlated, continuous, and real-time measurements of the circulating drugs' pharmacokinetics. The μ NEAB-patch is created following an introduced low-cost fabrication scheme, which transforms a shortened clinical-grade needle into a high-quality gold nanoparticle-based substrate for robust aptamer immobilization and efficient electrochemical signal retrieval. This enables the reliable in-vivo detection of a wide library of ISF analytes—especially, those with nonexistent natural recognition elements. Accordingly, we developed μ NEABs targeting various drugs, including antibiotics with narrow therapeutic windows (tobramycin and vancomycin). Through in-vivo animal

studies, we demonstrated the strong correlation between the ISF/circulating drug levels, and the device's potential clinical use for timely prediction of total drug exposure.

Teaser

A microneedle-based aptamer biosensor to measure the drug levels minimally-invasively and continuously in real-time

MAIN TEXT

Introduction

To realize precision and personalized medicine for effective pharmacotherapy, the right drug needs to be delivered to the right patient at the right dose and at the right time. In that regard, appropriate dosing for pharmaceuticals that present narrow therapeutic windows, such as antibiotics, is particularly challenging. In such cases, the high inter-/intra-subject variations—stemming from influential factors including kidney/liver function, tissue penetration, and drug-drug interactions—may often cause the drug level to fall outside the optimal therapeutic window. This can lead to adverse outcomes, such as kidney injury, and ineffective pharmacotherapy.

To circumvent such issues, patients who are prescribed these medications undergo therapeutic drug monitoring (TDM) sessions. At present, standard practices for conducting TDM involve invasive blood draws, followed by labor-intensive and high-cost lab-based analysis (e.g., chromatography, immunoassay) to capture the drug circulating level at one or two timepoint(s) (Fig. 1A) (1). These limitations severely compromise the utility of TDM for optimal dosing in many aspects. Firstly, the turnaround times for results are prolonged (~24 h), and thus, inadequate to allow for timely intervention. Secondly, the poor temporal resolution of the measurements (mostly confined to a single trough level measurement) inherently limit the accuracy of the current TDM approaches in terms of predicting the drug's highly complex pharmacokinetic (PK) characteristics (e.g., area-under-the-curve [AUC]) (2). Thirdly, because of their limited accessibility, TDM sessions are conducted at sub-optimal rates over the course of treatment, and subsequently fail to capture longitudinal variations in the drug's PK characteristics. This shortcoming is particularly critical for antibiotics-based treatments, where the antibiotic itself or the co-administered drugs can affect the drug clearance (e.g., due to the changes they make to renal function) (3). Also applicable to antibiotics-based treatments, these acknowledged challenges contribute to emerging antibiotic resistance: not only because of inadequate dosing, but also because of avoiding the use of the best choice of antibiotic due to the need for TDM and the fears of inducing toxicities (4).

Wearable biosensors targeting non-/minimally-invasively accessible biofluids can in principle address the limitations encountered in current TDM practices by enabling the seamless, continuous, and real-time measurement of the drug levels (5-9) (Fig. 1B). To this end, probing interstitial fluid (ISF) is a viable approach. A wide panel of pharmaceuticals partition into ISF with a high correlation to their circulating blood levels, many of which may not diffuse into other accessible biofluids such as sweat and saliva (10). Furthermore, probing ISF could be advantageous in the context of antibiotics-based treatments, given that the ISF compartment is often the intended site for drug activity, as it is in this space

where many bacterial infections start and progress. In such cases, the ISF-based measurements may provide a more direct insight as compared to the blood-based counterpart (11).

The molecular information in the ISF can be minimally-invasively retrieved with the aid of microneedle devices. These devices possess sharp, mechanically robust, and short needle-like features that enable easy and fracture-free skin penetration with no/minimal pain. By coupling electrochemical sensing capability with the microneedle's skin piercing functionality, microneedle devices can be adapted for the sample-to-answer quantification of ISF analytes in-skin (6, 12-14). However, the demonstrated microneedle-based electrochemical sensors rely on enzymes or ionophores for analyte recognition, excluding a wide variety of drug molecules for which these recognition elements are not available.

In that regard, the use of aptamers, as artificially engineered recognition elements, can greatly expand the library of detectable analytes (15). Although aptamer-based microneedles have been previously demonstrated, they are mostly geared at drug delivery (16) or multi-step sampling/ex-vivo affinity-based sensing (17). The latter group does not possess means for acquiring real-time in-vivo signals, and thus, they are incapable of charting the pharmacokinetic profile of the hypothetical target drugs accurately and providing timely and actionable feedback.

By immobilizing redox signal reporter-coupled aptamer molecules onto the surface of an electrode, an electrochemical aptamer biosensor (EAB) can be formed—which reversibly and in real-time transduces aptamer-target bindings into an electrically measurable signal (18, 19). Several EABs have been developed and adapted for the measurement of analytes in blood, illustrating the utility of this class of biosensors for complex biofluid analysis (18, 20, 21).

Toward reliable, real-time, continuous ISF biomonitoring, augmenting microneedles with EAB interfaces remains non-trivial. To elaborate, for robust EAB-based sensing, a high-quality surface (e.g., gold) is needed to ensure the strong covalent binding of the aptamer molecules (typically with the aid of an intermediary thiol group) and the efficient retrieval of the transduced signal (22). For the envisioned setting, the surface must be additionally resilient against the disruptive mechanical conditions involved in dermal applications (e.g., insertion-induced delamination), while satisfying electrochemical requirements (e.g., high sensitivity, anti-fouling) (23-25). Nevertheless, the most recent demonstrations of EAB microneedles suffer from poor signal-to-noise ratio (SNR) measurements and the degradation of the sensing layer during in-vivo operation, despite employing complex and costly fabrication schemes (26).

Addressing these challenges, here, we present a simple and low-cost EAB-on-microneedle fabrication scheme to develop a microneedle-based EAB patch (“ μ NEAB-patch”) for in-skin ISF biomonitoring (Fig. 1C). Our fabrication scheme centers on engineering a robust gold nanoparticle (AuNP) coating via a single deposition step, which uniquely transforms the surface of a clinical-grade needle into a high-quality gold working electrode for strong aptamer immobilization. Following this scheme, the sensing interfaces are built on the tip

of shortened acupuncture gold needles, allowing to simultaneously leverage the needles' high sharpness for skin penetration and conductivity for signal routing.

Illustrating the generalizability of our approach, we developed multiple μ NEABs targeting antibiotics (tobramycin and vancomycin) as well as other drugs (doxorubicin: an anticancer drug; thrombin: a procoagulant and anticoagulant). The antibiotic choice was motivated by noting their narrow therapeutic window (tobramycin: 4-21 μ M, 214-267 μ M·h [AUC] (27); vancomycin: 6-35 μ M, 276-414 μ M·h [AUC] (28)) and their high rate of treatment-induced kidney injuries (tobramycin: 12% (29); vancomycin: 24% (30)). It is worth noting that such injury rate can be effectively minimized via advanced TDM solutions (2).

Our characterization results indicate that the developed μ NEABs present a high level of sensitivity and stability (comparable to EABs developed on standard gold electrodes), while being suitable for intradermal applications. The in-vivo animal studies—which were performed with the tobramycin μ NEAB-patch on a rat model—revealed the high correlation of blood-ISF readings and the potential of real-time continuous ISF measurements for early prediction of critical circulating PK parameters that are commonly used to guide dosing (Fig. 1D). By reducing the feedback time for dosage adjustment from ~24 hours to minutes and obviating cumbersome and costly sample collection/analysis, our device serves as a viable, yet accessible TDM solution to maximize safety and optimize pharmacotherapy outcomes.

Results

To construct the μ NEAB-patch, we first fabricated microneedle electrodes by affixing clinical-grade acupuncture needles within a flexible polydimethylsiloxane (PDMS) substrate (fig. S1). This configuration leverages the needles' robustness and sharpness to reliably and painlessly pierce the stratum corneum layer of the skin, making it suitable for accessing dermal ISF analytes (31). Additionally, our mechanical characterization studies validated the high mechanical stability and robustness of the designed structure amid disruptive compression and shear forces relevant to the envisioned dermal application (Fig. S2A-C, performed following previously reported protocols (32, 33)).

To render real-time and continuous sensing, pharmaceutical-targeting aptamers are immobilized onto the microneedle electrode surface. The distal ends of the aptamers are tagged with redox-active molecules (methylene blue, MB) as signal reporters. The aptamers undergo reversible (18, 19) and rapid (in millisecond scales (34)) conformational changes upon binding to the target pharmaceutical. The aptamer conformational change alters the charge transfer rate between the signal reporter and electrode surface, which can be measured via voltammetry-based approaches.

As a key fabrication step of the μ NEAB-patch, we specifically engineered a low-cost AuNP-coated gold microneedle surface (denoted as AuNP-microneedle) to serve as the biosensor substrate. This coating is critical to the EAB construction and signal transduction. It minimizes substrate impurity (which comes hand in hand with the microneedle's low cost) and renders a high-quality surface for strong aptamer binding (via a self-assembled thiol group) (35, 36). Its nanostructured morphology effectively increases the area for

aptamer immobilization, which is useful for increasing the SNR of measurements (37, 38). Also, importantly, it secures a strong adhesion to the microneedle substrate (owing to the local galvanic reduction of gold ions during the electrodeposition) (39, 40), enabling device resilience against disruptive mechanical forces encountered in dermal settings (e.g., during insertion).

The surface chemistry of the AuNP-microneedle was first characterized and compared with that of the bare microneedle substrate (originally Au-plated). As shown in the scanning electron microscopy-energy dispersive spectroscopy (SEM-EDS, Fig. 2A), a high level of nickel (Ni) impurity was identified on a bare microneedle surface, while the AuNP coating effectively suppressed the Ni-associated peaks. Eliminating the Ni exposure is important, because Ni and its associated surface oxide layer can impede aptamer immobilization for signal retrieval (fig. S3). To further verify this point, representative tobramycin μ NEABs were constructed on both substrates and the biosensors' voltammetric readouts were recorded in a custom developed artificial ISF buffer environment. As shown in Fig. 2B(ii), for an AuNP-coated μ NEAB, a well-defined MB reduction peak with a flat baseline was observed, indicating the formation of a compact self-assembled monolayer (41). However, for the bare microneedle electrode, the voltammetric peak of the signal reporter is hardly differentiated from the background (Fig. 2B(i)). As shown in fig. S4, the comparison of the readouts of AuNP-deposited microneedle biosensors with Au-evaporated equivalents demonstrates the benefit of the AuNP coating in terms of enhancing the signal current, which is important for increasing the measurements' SNR and precision (37, 38).

To illustrate the generalizability of our approach, we developed additional microneedle-based EABs (targeting vancomycin, doxorubicin, and thrombin; in addition to tobramycin) by immobilizing the corresponding aptamers on the AuNP-microneedle substrates. As shown in Fig. 2C,D and fig. S5, for all four cases, the corresponding biosensor responses and analyte concentrations present a monotonic relationship with minimal inter-device variations. Here, relative peak current change was used to represent the sensor response in order to minimize inter-device variations (42).

Aligned with our aforementioned motivation of tobramycin PK monitoring, in the subsequent characterization experiments, we primarily focused on tobramycin sensing. Accordingly, we first compared the performance of the tobramycin μ NEAB with the tobramycin-EAB constructed on a standard gold disc electrode and found that the two possess similar sensitivity levels (Fig. 2C and fig. S6A). To verify that the tobramycin μ NEAB's electrochemical response originates from the binding of the target molecules to MB-tagged aptamers, we conducted a control study using aptamer-free devices, and additionally employed electrochemical impedance spectroscopy (43) to characterize the μ NEAB's response (fig. S6B-D). We also characterized our μ NEAB's response to an increasing/decreasing target concentration and demonstrated the μ NEAB's rapid and reversible sensing capability (fig. S7A, in-line with previously reported results (19)). Moreover, we studied the μ NEAB's selectivity against relevant interfering species. Figure S7B,C show that the tested biosensors' responses are minimally affected (< 5%) by the presence of common endogenous molecules and frequently co-administered drugs (here, ibuprofen, azithromycin; also relevant to vancomycin monitoring (44-47)).

Furthermore, we characterized the tobramycin μ NEAB from the standpoint of long-term stability and reproducibility. To investigate the biosensor's long-term stability, we recorded its baseline readout in an artificial ISF buffer under two extreme scenarios: repeated interrogation (1000 scans) and extended operation time (> 15 h). In both scenarios, the biosensor readouts presented $< 10\%$ drift (Fig. 2E), indicating that both the electrochemically-driven and time-dependent desorption of the self-assembled monolayer were minimal. Our characterization of different batches of the tobramycin μ NEABs yielded minimal inter-/intra-batch response variations, demonstrating the high reproducibility of the biosensor fabrication scheme (Fig. 2F).

Toward translation into in-vivo biomonitoring, we extended our device characterization by using ex-vivo models that mimic the envisioned intradermal ISF biosensing scenario.

To evaluate the biosensor's continuous response, we utilized a phantom gel setup and the complete μ NEAB-patch (consisting of the tobramycin aptamer-immobilized working electrode, a silver/silver chloride [Ag/AgCl] reference electrode, and a gold counter electrode, all microneedle-based). We specifically used three test gels pre-spiked with different tobramycin concentrations, collectively representing the analyte concentration variations in dermal ISF. We rotated through these test gels and recorded the response of the μ NEAB-patch continuously (with the device being inserted in the gels). As shown in Fig. 3A, the μ NEAB produced rapid (< 1 min) as well as highly stable and reversible responses to tobramycin, suggesting its high suitability for continuous ISF biomonitoring in tissue-like environments.

Furthermore, we characterized the μ NEAB performance in terms of its biofouling resistance. Biofouling is a major challenge for in-vivo biosensing as it can render biosensors (including EABs) unusable within a short period of time. For this characterization, we utilized two methods. The first method was based on characterizing the biosensor response in a protein-spiked buffer solution. For this study, to mimic the effect of large proteins, we followed a previously reported protocol (48), and spiked the artificial ISF buffer to contain 20 mg/mL bovine serum albumin (BSA, within the concentration range of common large proteins in the ISF). In this setting, the sensor exhibited a relatively small drift over ~ 14 h (both in the presence and absence of the flow; fig. S8A,B). The second method was based on characterizing the biosensor readout drift in a tissue environment, which was performed by continuously recording the biosensor readouts in a piece of rat or porcine skin. Figures 3B(i) and S8C show that the in-skin measurements stayed within $\sim 80\%$ of the initial measurement values for over 5 h of operation (comparable to previously reported results in a similar context (49)). Furthermore, comparison of the biosensor's response to tobramycin (10 μ M) before versus after the biofouling test revealed a statistically non-significant effect on the biosensor response ($p = 0.23$ in Fig. 3B(ii); $p = 0.24$ in fig. S8C).

Collectively, the biofouling characterization results indicate the preserved biosensing functionality of the μ NEAB within the envisioned measurement time window (corresponding to the drug's time-excision in the circulation ~ 2 -3 hours (50)). Relevant

to these experiments, we also verified the μ NEAB's preserved signal transduction in surrounding skin, by measuring its electrochemical impedance phase response in excised porcine skins, which were pre-soaked with tobramycin (fig. S6D). To further minimize drift and enable accurate readouts, the effect of confounders that may alter the EAB performance need to be systematically characterized (e.g., pH, ionic strength, surface adsorption of cells and biomolecules, and change of aptamer's binding kinetics in the tissue environment (22, 51)).

Additionally, we evaluated the influence of insertion-induced disruptions to the biosensor performance. Previous studies performed with microneedle-based biosensors indicated a significant degradation of the sensing layer upon insertion into the epidermis (26, 52). To characterize this effect in our context, we measured and compared the biosensor response to tobramycin (10 μ M) before and after repetitive insertions into a piece of porcine skin. As shown in Fig. 3C, the response remained relatively constant ($< 10\%$ variations), indicating the robustness of the coated/immobilized layers against insertion-induced disruptions. For comparison, we performed similar characterization studies using equivalent microneedle devices with Au-evaporated (instead of AuNP-deposited) metallic coating (as conventionally pursued in the fabrication of microneedle biosensors (26, 32)). Figure S9 shows that the readouts of the Au-evaporated microneedles were drastically reduced and that the devices completely lost their sensing functionality within a few insertions (attributable to the delamination of the evaporated gold coating). Furthermore, relevant to the envisioned dermal application, we characterized the stability of the μ NEAB-patch readout in the presence of motion, which may cause device delamination and signal distortion. As shown in fig. S2D, we observed negligible fluctuations in the patch readouts ($< 4\%$), despite the induced motion.

Moreover, we investigated the μ NEAB-patch's skin penetration capability. Figure 3D and fig. S10A show the hematoxylin and eosin (H&E) stained rat skin tissue after microneedle insertion, confirming that the developed microneedle device penetrated the epidermis and accessed the dermal layer of the skin. The difference between the observed insertion depth and the physical length of the devised microneedle can be attributed to the deformation of the surface of the viscoelastic skin and manual error in cutting the skin during the section processing (53).

We also evaluated the biocompatibility of the μ NEAB-patch. We first assessed the possibility of cell toxicity, stemming from the potential leaching of the needles' substances (e.g., AuNP, Ag/AgCl) into the surrounding medium. Accordingly, we cultured human dermal fibroblasts (HDFs) in the medium that was originally incubated with the microneedle electrode and then performed a trypan blue exclusion assay. As shown in Fig. 3E, the viability of the cells in the experiment groups (cells cultured in the medium incubated with the microneedle electrodes) presented statistically non-significant differences ($p > 0.12$) as compared to the respective control group (cells cultured in an untouched medium). Also, no noticeable change in the shape of the cells was observed in all the experiments. Similarly, we verified that when culturing the HDFs directly with the microneedle electrodes, the HDFs growth was unaffected by the microneedle electrodes' presence/contact. As shown in Fig. S11A, the HDFs near the electrodes maintained normal

morphology and no senescence was observable. Furthermore, to evaluate the μ NEAB-patch's skin biocompatibility, we affixed our device onto the dorsal skin of a live rat for the duration of three hours before harvesting the skin tissue. Figure S11B shows the photo of the insertion point, alongside with the control skin (no microneedle insertion), where no morphological abnormality (e.g., swelling, increased number of immune cells) was observed. Collectively, these results show no adverse effects on the cell/animal for the intended device operation time.

The developed μ NEAB-patch was then deployed in animal studies to monitor the PK profile of tobramycin in dermal ISF and investigate the drug's ISF-blood correlation. These experiments were performed on three healthy adult Sprague-Dawley rats. For these experiments, tobramycin was administered intravenously, while the rats were anesthetized, with the patch applied on their dorsal skin (Fig. 4A). Figure S10B shows no visible patch-induced bleeding as well as the rapid skin recovery upon the patch removal, reaffirming the minimally invasive nature of the developed technology.

To investigate the drug's ISF-blood correlation, blood samples were simultaneously collected before and at intermittent time points after the drug injection, and then analyzed by the standard lab instrument (liquid chromatography with tandem mass spectrometry, LC-MS/MS). The ISF PK measurements were interpreted with the aid of a two-compartment pharmacokinetic model that accounts for the drug distribution (from blood to ISF) and elimination (Fig. 4B). We investigated the relationship between the drug's circulating AUC (AUC_{blood}) and the processed μ NEAB-patch readouts—specifically, the area under the curve (AUC_{ISF}) and the maximal value of the sensor responses (R_{max}). The choice of AUC_{blood} was motivated by its common use (as a standard measure of total drug exposure) to guide dosing (27).

We first assessed the μ NEAB-patch's core capability of tracking the ISF PK profile in-vivo. As shown in fig. S12A, upon a bolus tobramycin injection (20 mg/kg), a rapid increase, followed by a gradual decrease in sensor readout was observed, corresponding to the drug's distribution and redistribution/elimination phases. In a separate vehicle control experiment, the injection of a similar amount of saline (vehicle of the drug) did not induce noticeable AUC_{ISF} (fig. S12B, $AUC_{\text{ISF}} = 0.099 \% \cdot \text{h}$, within 80 min post injection). The results suggest that the injection event and the long-term anesthesia have minimal confounding effects on the sensor response. To assess the generalizability of our solution for in-vivo biomonitoring, we performed a proof-of-concept vancomycin biomonitoring experiment using the respective μ NEAB-patch. The captured vancomycin profile in ISF (fig. S13) presented a similar drug distribution/elimination pattern as that observed in previously reported vancomycin studies, which were performed via manual ISF sampling and off-body analysis (54)).

Next, we extended the study to investigate the tobramycin's PK characteristics in relation to the administered drug dosages (performed on three rats). For each rat, we performed the associated experiments with at least one week interval to avoid carryover effects. As shown in Fig. 4C, fig. S14, and fig. S15, both R_{max} and AUC_{ISF} increased with the increase of drug

dosages for all three animals. Through analysis of blood samples, we found out this trend was also reflected by the AUC_{blood} (Fig. 4D, S15B-D).

Figure 4E tabulates the collective results obtained from a total of nine independent trials (performed on three rats). It should be noted that for the same animal, neither the blood-based nor the ISF-based drug measurements were linearly proportional to the correspondingly administered dosage. Furthermore, the animals' response to the same injection dosage (e.g., 20 mg/kg) varied significantly (AUC_{blood} : $180 \pm 112 \mu\text{M} \cdot \text{h}$; AUC_{ISF} : $7.7 \pm 6.2 \% \cdot \text{h}$). These observations indicate high degrees of inter-/intra-subject variations (in line with previously reported blood-based results (55)), which can be attributed to variations in the rats' underlying physiological conditions (e.g., renal function, weight, diet) (3, 56).

Encouragingly, despite these variations, the μNEAB -patch-generated ISF readouts captured the circulating pharmacokinetic characteristics reliably. Figure 4F shows the high level of correlation between AUC_{blood} and AUC_{ISF} ($R^2 = 0.99$) as well as AUC_{blood} and R_{max} ($R^2 = 0.97$). These results suggest that the real-time continuous ISF readings rendered by our μNEAB -patch can be leveraged to predict the subject's total drug exposure for precision dosing (albeit it must be noted the prediction error for R_{max} increases at higher concentrations). The corresponding Bland-Altman plots for these measurements are shown in fig. S16A,B. Specifically, when the maximum response value is used, the feedback time can be reduced to ~ 15 min (fig. S16C). This provides the possibility of finetuning the dosage within the intended therapeutic window and/or the time interval to next dosing administration.

Discussion

The ex-vivo and in-vivo characterization results comprehensively support the suitability of the μNEAB -patch for tracking the drug's pharmacokinetics minimally-invasively and in real time. The μNEAB -patch renders high SNR measurements over prolonged in-vivo operations. This is achieved by uniquely leveraging the enabling features of the AuNP coating that facilitates a strong adhesion to the microneedle substrate and an increased area for aptamer immobilization. The AuNP coating is realized by an introduced fabrication scheme, which transforms a widely-used clinically-grade needle (optimized for dermal application) into a high quality in-vivo biosensor, while only requiring a simple deposition step, with an added cost of a few cents (Table S1; total device material cost \sim \$2). These enabling attributes of the devised fabrication scheme allow for simultaneously overcoming the limitations of previous microneedle biosensors and minimizing the barriers to clinical translation, mass production, and eventual large-scale deployment/adoption of the device (10, 23).

The continuous ISF analyte readouts rendered by this patch revealed the high correlation of AUC_{ISF} and R_{max} with respect to the animal's total drug exposure. These results demonstrate the potential clinical utility of our solution for precision dosing. In particular, the use of R_{max} , as an indicator of drug exposure, could be of tremendous value. It reduces the time for extracting the drug's circulating pharmacokinetics from several hours (time-to-trough: ~ 12 h; sample analysis: ~ 6 -12 h) to minutes. In this way, the presented

technology uniquely enables timely feedback for dosage adjustment and other interventions such as extending the time interval for dosing. This will effectively maximize the treatment efficacy, while minimizing toxicities and adverse effects. It is also worth highlighting the large inter-/intra-subject variations observed in the antibiotics' circulating pharmacokinetics (similar to previous findings). These observations further emphasize the pressing need for performing TDM at a higher frequency and with an improved accuracy, aligned with the possibilities offered by our technology.

Toward translating this technology into clinical settings, dedicated engineering and clinical efforts are needed. While here we mainly focused on studying the performance of the developed tobramycin μ NEAB, additional engineering efforts are needed to evaluate and optimize the in-vivo performance of the other μ NEABs (e.g., vancomycin) that are introduced in this work. Furthermore, existing commercial wearable packaging/system integration solutions can be adopted to form a fully-integrated wireless patch, given that our patch is compact (~6 mm in diameter) and light (0.5 g), and in principle requires the same grade of electronics for wireless operation as those used in commercial solutions (e.g., continuous glucose monitoring devices). The technology could particularly benefit from surface engineering methods (49), differential/auxiliary measurement techniques (18), and corrective algorithms that minimize error caused by ISF-specific confounding factors (e.g., biofouling-induced drift within a tissue environment). Furthermore, standard microneedle sensor calibration methodologies are needed to benchmark the biosensor performance in the ISF environment. To this end, the findings from recently introduced ISF analyte sampling/analysis techniques are insightful and have formed a solid foundation for building such methodologies (6, 10, 57). Moreover, large-scale clinical studies are needed to assess the ISF-blood correlation across different patient populations. These studies could benefit from advanced machine learning algorithms and data analytics approaches that render personalized models for precision dosing (1, 27).

The convergence of these efforts can establish an unprecedented wearable TDM modality. This modality directly addresses the problem of inappropriate drug dosing, which is a major cause of complications in antibiotics-based treatments. For tobramycin and vancomycin alone, these complications cause >40,000 acute kidney injuries and >\$5B treatment cost per year in the US (2, 30). Recent studies have estimated that improvements in the accuracy of employed TDM methods can reduce these adverse outcomes by 3-fold (2). In addition, the availability of a more practical TDM platform could also facilitate the access to drug regimens with higher chances of efficacy as opposed to the selection of alternative agents. The latter approach is often used in current medical practice to avoid the demands of TDM, but at the same time brings higher chances of failure as well as possibility of inducing antibiotic resistance (in the case of antibiotics). Therefore, we anticipate that the optimization and adoption of our technology can greatly promote enhanced pharmacotherapy outcomes with consequent improvements in the quality of life for large groups of patients as well as significant savings in healthcare costs. Furthermore, the presented technology can be adapted to monitor a wide range of clinically informative analytes (e.g., markers of disease and well-being). Thus, it can be broadly applied in a variety of biomonitoring settings (e.g., ISF biomarker investigations, large-scale clinical

trials, and telehealth) and for various biomedical applications in order to advance personalized and precision medicine.

Materials and Methods

Materials and Reagents. All reagents were purchased from Sigma-Aldrich (MO, USA) unless stated. Tris(2-carboxyethyl)phosphine hydrochloride (TCEP) was purchased from TCI America, Inc. (OR, USA). The human α -thrombin was purchased from Haematologic Technologies, Inc. (VT, USA). Tobramycin (900 $\mu\text{g}/\text{mg}$) and phosphate buffered saline (1 \times , Gibco PBS, pH 7.2) were purchased from Thermo Scientific (MA, USA). Tobramycin and vancomycin aptamers were purchased from Integrated DNA Technologies, Inc. (IA, USA) and doxorubicin and thrombin aptamers were purchased from Biosearch Technologies, Inc. (CA, USA). PDMS (Sylgard 184 Silicone Elastomer) was purchased from Dow Corning (MI, USA). Gold-plated acupuncture needles were purchased from Suzhou Acupuncture & Moxibustion Appliance Co., Ltd (Suzhou, China). The lancets (30 gauge) were purchased from CVS pharmacy (RI, USA). Disc gold electrodes (diameter: 1.6 mm) were purchased from Bioanalytical Systems, Inc. (IN, USA). Silver-silver chloride (Ag/AgCl) ink was purchased from Ercon Incorporated (MA, USA).

μNEAB -patch fabrication. The μNEAB -patch consists of three repurposed microneedle electrodes, a PDMS substrate, and a 3D-printed case (as the housing of the μNEAB -patch). The PDMS substrate was fabricated by mixing the base and the curing agent at a 10:1 ratio. The mixture was subsequently poured into a petri dish (thickness: ~ 3 mm) and cured at 70 $^{\circ}\text{C}$ for 5 h. The cured PDMS was then cut and embedded within the cylindrical 3D-printed case (diameter: 6 mm, height: 5 mm). The solid needles were inserted into the PDMS substrate with the aid of a custom-designed mold to form a microneedle-based three-electrode configuration (exposed tip length: ~ 1 mm; base diameter: 350 μm ; separation between electrodes: ~ 2 mm). Flexible wires were used and soldered to the distal end of the microneedle electrodes to establish connection with the potentiostat. The whole device was sealed by epoxy.

The working and counter electrodes were constructed using gold-plated acupuncture needles. The needles were cleaned by sonication in ethanol followed by deionized (DI) water (5 min for each solvent). To form an AuNP-microneedle, the microneedle electrode was immersed in a stirring solution containing 1.2 mg/mL chloroauric acid (HAuCl_4), 0.1 M sodium chloride (NaCl), and 1.5 wt.% hydrochloric acid (HCl). A 30-mL volume of the prepared solution can be used to coat about 100 microneedles. A pulsed waveform of 0 V and -0.4 V (versus Ag/AgCl) was applied for 120 cycles (one cycle: 1 s for each potential) to form an AuNP coating (33). A bare microneedle (with an originally Au-plated surface) was directly used as a counter electrode. The reference electrode was constructed by dip-coating a lancet with Ag/AgCl ink (1:1 diluted in toluene) before inserting into the PDMS substrate.

Characterization of microneedle electrode surface morphologies and chemical compositions. The bare microneedle and AuNP-microneedle morphologies were characterized by SEM (ZEISS Supra 40VP). Surface chemical compositions were

characterized by EDS (Thermo Noran System 6). The size of the deposited AuNP was quantified by analyzing the SEM images using ImageJ (268 ± 56 nm).

Characterization of microneedle mechanical stability. The compression experiment of the microneedle device was performed in a universal testing machine (MultiTest 2.5-i, Mecmesin Ltd.) with a loading rate of 1 mm/min. The shear load experiment was performed using another universal testing machine (5966, Instron Inc.) with a loading rate of 0.5 mm/min. A ten-layer stacked parafilm was used to mimic the skin for the needle to puncture through (32). The loading and unloading data were recorded for both tests to show mechanical reversibility. The characterization of the device's structural stability against skin injection was performed by inserting the needle into a porcine skin for 20 times and measuring the needle's length with the aid of optical microscopy.

DNA aptamer sequences. The sequence of the aptamer probes used in the experiments are listed below:

Tobramycin:

5'-/5ThioMC6-D/GGGACTTGGTTTAGGTAATGAGTCCC/3MeBIN/-3' (30);

Vancomycin:

5'-/5ThioMC6-D/CGAGGGTACCGCAATAGTACTTATTGTTCGCCTATTGTGGGTCGG/3MeBIN/-3' (18);

Doxorubicin:

5'-/5ThioMC6-D/ACCATCTGTGTAAGGGGTAAGGGGTGGT/3MeBIN/-3' (34);

Thrombin:

5'-/5ThioMC6-D/TAAGTTCATCTCCCCGGTTGGTGTGGTTGGT/3MeBIN/-3' (35).

EAB fabrication. To fabricate EABs, a 5 μ L aliquot of the 100 μ M aptamer stock solution was thawed to room temperature and then reduced for 1 hour in the dark with 10 μ L of TCEP solution. The TCEP solution was prepared in a Tris buffer solution containing 100 mM Tris hydrochloride, 140 mM NaCl, 20 mM magnesium chloride ($MgCl_2$), and 20 mM potassium chloride (KCl). 100 mM TCEP was used to fabricate doxorubicin EABs while other EABs were fabricated with 10 mM TCEP (to achieve a lower probe density in the fabricated EABs). The TCEP-reduced aptamer was then diluted in 500 μ L PBS. To construct aptamer sensors on disc gold electrodes, the electrodes were electrochemically-cleaned following the previously reported method (41). The cleaned disc electrodes or the freshly-prepared microneedle electrodes were immersed in aptamer solution for 2 h at room temperature in the dark. Following this, the sensors were immersed overnight at room temperature in 20 mM 6-mercapto-1-hexanol (MCH, prepared in PBS) to coat the remaining gold surface and to remove non-specifically adsorbed aptamers. After this, the sensors were rinsed with DI water and stored in the artificial ISF buffer solution. To construct the control aptamer-free device, the freshly-prepared AuNP-microneedle electrode was immersed in 20 mM MCH (prepared in PBS) overnight at room temperature, followed by rinse with DI water.

Ex-vivo μ NEAB characterization. All the electrochemical measurements were performed using a CHI660E or a CHI1040C electrochemical workstation (CH Instruments, Inc., TX,

USA). The ex-vivo sensor characterizations were performed in an electrochemical cell (reference electrode: Ag/AgCl, counter electrode: platinum) containing artificial ISF buffer solution. The artificial ISF solution was prepared according to the previously reported composition (58). Here, 6.3 g NaCl (107.7 mM), 0.26 g KCl (3.5 mM), 0.17 g calcium chloride (CaCl₂, 1.5 mM), 0.17 g magnesium sulfate (MgSO₄, 0.7 mM), 2.2 g sodium bicarbonate (NaHCO₃, 26.2 mM), 0.26 g monosodium phosphate (NaH₂PO₄, 1.7 mM), and 2.1 g sodium gluconate (9.6 mM) were mixed in 1 L DI water and the pH was adjusted to 7.4. All sensors were interrogated using square wave voltammetry (SWV) with a frequency of ~200 Hz, a pulse amplitude of 25 mV, and a voltage increment of 1 mV. The acquired voltammograms were processed using Matlab (MathWorks, MA, USA) (similar to a previously reported method (59)). Specifically, to extract the voltammetric peak height information (which serves as our sensor readout), a linear baseline was first fitted to the corresponding local minimum current points at the two feet of the peak in the captured voltammogram. The peak current was extracted by subtracting the fitted baseline from the voltammogram and then sampling the resultant maximum value (e.g., as shown in fig. S4A).

For electrochemical impedance spectroscopy, the formal potential E_0 of the redox probe (i.e., MB) was first determined by cyclic voltammetry scanning (-0.1 V - -0.45 V, scan rate: 100 mV/s) in the respective test matrix. E_0 was defined as the midpoint between the oxidation and reduction peaks of the voltammogram. The impedimetric measurement was then performed by setting the bias point to E_0 and applying an AC potential waveform of 10 mV amplitude (frequency range: 10 kHz to 1 Hz).

To construct the phantom gels, 1.4 wt.% agarose powder (9) was mixed with artificial ISF solutions (containing tobramycin with various levels) and placed in an 80 °C water bath. After agarose was completely dissolved, the solutions were cooled to room temperature to form phantom gels. The fabricated μ NEAB-patch was inserted into the phantom gels and the sensor was interrogated continuously (with the interrogation paused during μ NEAB-patch transfer). To test the sensor drift in an ex-vivo setting, the μ NEABs were inserted into an excised porcine skin (Stellen Medical, MN, USA) and the biosensor readouts were monitored continuously. The skin was placed at the bottom of a beaker containing artificial ISF solution to prevent dehydration. The skin insertion test was performed by placing the μ NEABs into an excised porcine skin followed by an immediate withdrawal (serving as one insertion). The biosensors' responses to tobramycin were tested in an electrochemical cell (containing artificial ISF buffer solution) before and after skin insertions.

To test the sensor/device stability in the presence of motion, a μ NEAB-patch was inserted into a piece of rat skin and attached to a vortex mixer (Fisher Scientific). The vortex mixer was adjusted to mimic 3D oscillatory acceleration conditions (~10 m/s² at ~8 Hz, generated by the vortex mixer, following our previously reported wearable device characterization protocol (60)). The μ NEAB-patch was connected to a potentiostat to continuously record its readout. The three-dimensional acceleration data was measured by a smartphone.

Skin penetration efficiency test. The penetration test was performed on the rat skin immediately after the euthanasia of the animal (the carcass was donated by the Division of

Laboratory Animal Medicine at University of California, Los Angeles under a tissue sharing program to reduce the number of animals used). The hair on the lower back was removed by a depilation (Nair, Church & Dwight, NJ, USA) before the microneedle test was administered. The skin was penetrated multiple times with the developed microneedle, harvested, and fixed in 10% formalin (48 h). The fixed skin was paraffin embedded and sectioned. Sections (4 μm in thickness) were collected every 20 μm throughout the sample and stained with H&E.

In-vitro biocompatibility test. The cell toxicity test was performed using human dermal fibroblasts (61). The fabricated needle-based working, reference, and counter electrodes were separately incubated in three vials of Dulbecco's Modified Eagle Medium (DMEM, Thermo Scientific, MA, USA) in a CO₂ incubator (4 and 8 hours). The electrode incubation time is selected to span beyond the drug' half-life (~ 2-3 hours for tobramycin (50)). After the incubation, the electrodes were removed, the resultant DMEM was mixed with serum (up to 10% fetal bovine serum, FBS) and the cells (100,000 cells/well), and the mixture was plated. The plated cells were incubated at 37 °C in 5% CO₂ atmosphere (24 hours). After the incubation, all cells on the plate were collected by trypsinization. Cell viability was determined by trypan blue stain using the hemocytometer. Trypan blue is cell membrane impermeable and only enters cells with compromised membranes. Thus, the staining of a cell indicates its death (62). In a separate experiment, the microneedle electrodes and HDFs were placed on the bottom of the cell culture dish and the dish was plated with HDFs and the images were taken after 24 and 48 hours.

Skin biocompatibility test. We performed the skin biocompatibility test by putting the animal (here, rat) under anesthesia and affixing the microneedle electrode array (5×5 microneedles) on the dorsal skin. The animal was then allowed free movement for 3 hours. Then, the microneedle electrode array was removed, and the animal was euthanized. The skin was collected immediately after the euthanasia and fixed in the 10% formalin. The fixed skin was paraffin embedded and sectioned. Sections (4 μm in thickness) were collected every 40 μm and stained with H&E.

In-vivo μ NEAB-patch characterization on a rat model. The animal study protocol was reviewed and approved by the Institutional Animal Care and Use Committee (IACUC) at University of California, Los Angeles. Four adult female Sprague-Dawley rats were purchased from Charles River Laboratories International, Inc. (MA, USA) (weight at the point of experiment: 300-400 g). Rats were housed in the facility (1 or 2 rats per cage) with controlled temperature and humidity on a 12-h light-dark cycle with food and water available ad libitum throughout the studies. A minimal seven-day acclimate time was provided before any procedure was implemented.

In the drug monitoring experiment, the rat was under isoflurane anesthesia (1.5% - 2%) with a circulating heating pad to maintain its body temperature at ~ 37 °C. A peripheral venous catheter was placed into the tail vein right after anesthesia to facilitate intravenous drug injection. A μ NEAB-patch was applied onto the rat's lower back (with hair removed) and a Tegaderm film (3M, MN, USA) was used to secure the device in place. The suitability of this film for interfacing wearable devices with skin has been demonstrated by numerous

previous studies (60, 63). The μ NEAB-patch was connected to a potentiostat to provide real-time readouts. The biosensor was interrogated using the same method and parameters as the ex-vivo experiments (with ~ 30 s interval between measurements). The biosensor baseline was monitored for at least 1 h before drug injection. Venous blood was collected from the tail vein or the lateral saphenous vein before and at intermittent time points after drug injection. Blood was left undisturbed at room temperature for 15 min, and then centrifuged at 10,000 rpm for 10 min. The supernatant (serum) was stored at -20 °C before analysis. To administer the tobramycin, the tobramycin stock solution (40 mg/mL, Baxter International, IL, USA) was diluted with saline (Hospira, IL, USA) to a final volume of ~ 1 mL and slowly injected into the vein via the catheter. Similarly, to administer the vancomycin, the lyophilized vancomycin hydrochloride (1g per vial, Almaject Inc., NJ, USA) was mixed with saline to form a clear solution (100 mg/mL) and injected into the vein via catheter.

Data analysis for in-vivo experiments. In-vivo experiment data was analyzed using Matlab. First, the MB redox peak currents were extracted from recorded voltammograms using the same method as the ex-vivo experiments. Continuous sensor readout $I_{readout}(t)$ was subsequently constructed. To correct for the sensor baseline drift, a hypothetical baseline $I_{baseline}(t)$ was constructed using an exponential equation (previously used to describe the EAB readout drift pattern in biofluid (51)). The baseline was fitted using the pre-injection sensor readouts, while ensuring all the post-injection readouts were above the fitted baseline. The sensor response $r(t)$ was defined as:

$$r(t) = \frac{I_{readout}(t) - I_{baseline}(t)}{I_{baseline}(t)} \times 100\% \quad (1)$$

Pharmacokinetic analysis. The pharmacokinetic analysis was performed based on a two-compartment pharmacokinetic model (64). Accordingly, the continuously recorded sensor response was fitted using a bi-exponential equation derived from the model:

$$C_{ISF} = X[e^{-\beta t} - e^{-\alpha t}] \quad (2)$$

, where α and β are related to the distribution and elimination rates, respectively, and X is the pre-exponential factor. Applicable to our in-vivo studies, in the context of intravenous bolus administration, it can be assumed that the drug concentration in blood immediately peaks upon injection as it is rapidly distributed, and then gradually declines as the drug is eliminated (64). Here, due to the limited number of blood samples acquired per trial, the blood concentration versus time curve was fitted using a simplified exponential equation to avoid overfitting:

$$C_{blood} = Y e^{-\gamma t} \quad (3)$$

, where γ is predominantly determined by the drug elimination rate and Y is the pre-exponential factor. The AUC and R_{max} information were extracted from the fitted pharmacokinetic profiles. In case of the need for establishing the point-to-point correlation of ISF and blood readings and unifying the expressions (2) and (3), the consideration of the analyte blood-ISF transport delay may be necessary (67). To construct Bland-Altman plots, the AUC_{blood} was predicted based on the AUC_{ISF} and R_{max} information derived from the μ NEAB-patch readouts. The data from one trial were utilized to calibrate the remaining measurements.

Tobramycin quantification with LC-MS/MS. The tobramycin concentrations in the rat serum were quantified using LC-MS/MS with a multiple reaction monitoring (MRM) technique (55). Sisomicin sulfate was used as the internal standard (IS). For calibration, tobramycin stock solution was prepared in DI water at a concentration of 1 mg/mL. The stock solution was further diluted with DI water to obtain calibration standards at 0, 100, 200, 500, 1000, and 1500 ng/mL. The IS stock solution was prepared in DI water at a concentration of 1 mg/mL and was further diluted with water to 10 µg/mL. 5 µL of the rat serum samples was first diluted into 445 µL of DI water. 50 µL of 10 µg/mL IS was then spiked into 450 µL of calibration standards or diluted serum samples (to reach a final IS concentration of 1 µg/mL). The resultant samples were mixed and vortexed with 500 µL acetonitrile, followed by centrifugation at 14,800 rpm for 10 min. 1 mL of the supernatant was mixed and vortexed with 500 µL of dichloromethane, followed by centrifugation at 14,800 rpm for 10 min. Then, 400 µL of the new supernatant was mixed and vortexed with 400 µL of DI water, followed by centrifugation at 14,800 rpm for 10 min. Finally, 100 µL of the supernatant was transferred into an autosampler vial for tobramycin quantification.

For HPLC analysis, Agilent 1200 series HPLC (Agilent Technologies, CA, USA) equipped with HTS PAL autosampler (CTC Analytics, MN, USA) was coupled to an API 4000 triple quadrupole mass spectrometer (Sciex, ON, Canada) for MRM experiments. Chromatographic separation was realized by the InfinityLab Poroshell 120 EC-C18 (3.0×50 mm, 2.7 µm, Agilent Technologies). The mobile phases A and B were water and acetonitrile respectively, both mixed with 10 mM heptafluorobutyric acid (HFBA). The flow rate was set at 400 µL/min with 3 minutes of equilibrium time. The gradient starts with increasing B from 5% to 90% in 4 minutes (0-4 min), then maintaining 90% B for 4 minutes (4-8 min), followed by decreasing B from 90% to 5% in 1 minute (8-9 min), and finally maintaining 5% B for 3 minutes (9-12 min). Sample vials were maintained at 4 °C in the autosampler tray. 20 µL of sample was loaded onto the column each time. The tandem mass spectrometry was operated in MRM mode recording the following *m/z* transitions: 468.4 → 163.2 for tobramycin and 448.3 → 160.2 for sisomicin. The declustering potential, entrance potential, collision energy, and collision cell exit potential were optimized at 86 V, 10 V, 35 V, and 10 V for tobramycin and 76 V, 10 V, 29 V, and 10 V for sisomicin.

References and notes

1. H. C. Ates, J. A. Roberts, J. Lipman, A. E. G. Cass, G. A. Urban, C. Dincer, On-Site Therapeutic Drug Monitoring. *Trends Biotechnol.* **38**, 1262-1277 (2020).
2. B. V. Lee, G. Fong, M. Bolaris, M. Neely, E. Minejima, A. Kang, G. Lee, C. L. Gong, Cost-benefit analysis comparing trough, two-level AUC and Bayesian AUC dosing for vancomycin. *Clin Microbiol Infect* **27**, (2021).
3. D. N. Gilbert, C. Plamp, P. Starr, W. M. Bennett, D. C. Houghton, G. Porter, Comparative Nephrotoxicity of Gentamicin and Tobramycin in Rats. *Antimicrob. Agents Chemother.* **13**, 34-40 (1978).
4. B. C. P. Koch, A. E. Muller, N. G. M. Hunfeld, B. C. M. de Winter, T. M. J. Ewoldt, A. Abdulla, H. Endeman, Therapeutic Drug Monitoring of Antibiotics in Critically Ill Patients: Current Practice and Future Perspectives With a Focus on Clinical Outcome. *Ther Drug Monit.* **44**, 11-18 (2022).

5. S. Lin, W. Yu, B. Wang, Y. Zhao, K. En, J. Zhu, X. Cheng, C. Zhou, H. Lin, Z. Wang, H. Hojaiji, C. Yeung, C. Milla, R. W. Davis, S. Emaminejad, Noninvasive wearable electroactive pharmaceutical monitoring for personalized therapeutics. *Proc. Natl. Acad. Sci. U.S.A.* **117**, 19017-19025 (2020).
6. T. M. Rawson, S. A. N. Gowers, D. M. E. Freeman, R. C. Wilson, S. Sharma, M. Gilchrist, A. MacGowan, A. Lovering, M. Bayliss, M. Kyriakides, P. Georgiou, A. E. G. Cass, D. O'Hare, A. H. Holmes, Microneedle biosensors for real-time, minimally invasive drug monitoring of phenoxymethylpenicillin: a first-in-human evaluation in healthy volunteers. *Lancet Digit Health* **1**, e335-e343 (2019).
7. H. Teymourian, M. Parrilla, J. R. Sempionatto, N. F. Montiel, A. Barfidokht, R. Van Echelpoel, K. De Wael, J. Wang, Wearable Electrochemical Sensors for the Monitoring and Screening of Drugs. *ACS Sens.* **5**, 2679-2700 (2020).
8. L. C. Tai, T. S. Liaw, Y. J. Lin, H. Y. Y. Nyein, M. Bariya, W. B. Ji, M. Hettick, C. S. Zhao, J. Q. Zhao, L. Hou, Z. Yuan, Z. Y. Fan, A. Javey, Wearable Sweat Band for Noninvasive Levodopa Monitoring. *Nano Lett.* **19**, 6346-6351 (2019).
9. R. K. Mishra, K. Y. Goud, Z. H. Li, C. Moonla, M. A. Mohamed, F. Tehrani, H. Teymourian, J. Wang, Continuous Opioid Monitoring along with Nerve Agents on a Wearable Microneedle Sensor Array. *J. Am. Chem. Soc.* **142**, 5991-5995 (2020).
10. J. Heikenfeld, A. Jajack, B. Feldman, S. W. Granger, S. Gaitonde, G. Begtrup, B. A. Katchman, Accessing analytes in biofluids for peripheral biochemical monitoring. *Nat. Biotechnol.* **37**, 407-419 (2019).
11. O. Cars, Pharmacokinetics of Antibiotics in Tissues and Tissue Fluids - a Review. *Scand. J. Infect. Dis.* **74** (suppl), 23-33 (1991).
12. W. Lee, S. H. Jeong, Y. W. Lim, H. Lee, J. Kang, H. Lee, I. Lee, H. S. Han, S. Kobayashi, M. Tanaka, B. S. Bae, Conformable microneedle pH sensors via the integration of two different siloxane polymers for mapping peripheral artery disease. *Sci. Adv.* **7**, eabi6290 (2021).
13. M. Parrilla, M. Cuartero, S. P. Sanchez, M. Rajabi, N. Roxhed, F. Niklaus, G. A. Crespo, Wearable All-Solid-State Potentiometric Microneedle Patch for Intradermal Potassium Detection. *Anal. Chem.* **91**, 1578-1586 (2019).
14. S. Sharma, A. El-Laboudi, M. Reddy, N. Jugnee, S. Sivasubramaniyam, M. El Sharkawy, P. Georgiou, D. Johnston, N. Oliver, A. E. G. Cass, A pilot study in humans of microneedle sensor arrays for continuous glucose monitoring. *Anal. Methods* **10**, 2088-2095 (2018).
15. J. O. Lee, H. M. So, E. K. Jeon, H. Chang, K. Won, Y. H. Kim, Aptamers as molecular recognition elements for electrical nanobiosensors. *Anal. Bioanal. Chem.* **390**, 1023-1032 (2008).
16. J. Cao, J. J. Su, M. C. An, Y. Yang, Y. Zhang, J. Zuo, N. Zhang, Y. X. Zhao, Novel DEK-Targeting Aptamer Delivered by a Hydrogel Microneedle Attenuates Collagen-Induced Arthritis. *Mol. Pharm.* **18**, 305-316 (2021).
17. K. X. Yi, Y. T. Wang, K. Q. Shi, J. J. Chi, J. X. Lyu, Y. J. Zhao, Aptamer-decorated porous microneedles arrays for extraction and detection of skin interstitial fluid biomarkers. *Biosens. Bioelectron.* **190**, 113404 (2021).
18. N. Arroyo-Curras, J. Somerson, P. A. Vieira, K. L. Ploense, T. E. Kippin, K. W. Plaxco, Real-time measurement of small molecules directly in awake, ambulatory animals. *Proc. Natl. Acad. Sci. U.S.A.* **114**, 645-650 (2017).

19. B. S. Ferguson, D. A. Hoggarth, D. Maliniak, K. Ploense, R. J. White, N. Woodward, K. Hsieh, A. J. Bonham, M. Eisenstein, T. E. Kippin, K. W. Plaxco, H. T. Soh, Real-Time, Aptamer-Based Tracking of Circulating Therapeutic Agents in Living Animals. *Sci. Transl. Med.* **5** (213), 213ra165-213ra165 (2013).
20. P. L. Mage, B. S. Ferguson, D. Maliniak, K. L. Ploense, T. E. Kippin, H. T. Soh, Closed-loop control of circulating drug levels in live animals. *Nat. Biomed. Eng.* **1** (5), 1-10 (2017).
21. P. Dauphin-Ducharme, K. Yang, N. Arroyo-Curras, K. L. Ploense, Y. M. Zhang, J. Gerson, M. Kurnik, T. E. Kippin, M. N. Stojanovic, K. W. Plaxco, Electrochemical Aptamer-Based Sensors for Improved Therapeutic Drug Monitoring and High-Precision, Feedback-Controlled Drug Delivery. *ACS Sens.* **4**, 2832-2837 (2019).
22. N. Arroyo-Curras, P. Dauphin-Ducharme, K. Scida, J. L. Chavez, From the beaker to the body: translational challenges for electrochemical, aptamer-based sensors. *Anal. Methods* **12**, 1288-1310 (2020).
23. H. Teymourian, F. Tehrani, K. Mahato, J. Wang, Lab under the Skin: Microneedle Based Wearable Devices. *Adv. Healthc. Mater.* **10** (17), 2002255 (2021).
24. P. Yanez-Sedeno, S. Campuzano, J. M. Pingarron, Pushing the limits of electrochemistry toward challenging applications in clinical diagnosis, prognosis, and therapeutic action. *Chem. Commun.* **55**, 2563-2592 (2019).
25. W. Y. Yang, Y. Gong, W. Li, A Review: Electrode and Packaging Materials for Neurophysiology Recording Implants. *Front. Bioeng. Biotechnol.* **8**, 31 (2021).
26. Y. Wu, F. Tehrani, H. Teymourian, J. Mack, A. Shaver, M. Reynoso, J. Kavner, N. Huang, A. Furnidge, A. Duvvuri, Y. H. Nie, L. M. Laffel, F. J. Doyle, M. E. Patti, E. Dassau, J. Wang, N. Arroyo-Curras, Microneedle Aptamer-Based Sensors for Continuous, Real-Time Therapeutic Drug Monitoring. *Anal. Chem.* **94**, 8335-8345 (2022).
27. J. M. Brockmeyer, R. T. Wise, E. B. Burgener, C. Milla, A. Frymoyer, Area under the curve achievement of once daily tobramycin in children with cystic fibrosis during clinical care. *Pediatr. Pulm.* **55**, 3343-3350 (2020).
28. M. Rybak, B. Lomaestro, J. C. Rotschafer, R. Moellering, Jr., W. Craig, M. Billeter, J. R. Dalovisio, D. P. Levine, Therapeutic monitoring of vancomycin in adult patients: a consensus review of the American Society of Health-System Pharmacists, the Infectious Diseases Society of America, and the Society of Infectious Diseases Pharmacists. *Am. J. Health Syst. Pharm.* **66**, 82-98 (2009).
29. F. Paquette, A. Bernier-Jean, V. Brunette, H. Ammann, V. Lavergne, V. Pichette, S. Troyanov, J. Bouchard, Acute Kidney Injury and Renal Recovery with the Use of Aminoglycosides: A Large Retrospective Study. *Nephron* **131**, 153-160 (2015).
30. InsightRX, "2020 Vancomycin Dosing Guidelines - InsightRX White Paper" (2020, content.insight-rx.com/vancowp).
31. M. Rajabi, N. Roxhed, R. Z. Shafagh, T. Haraldson, A. C. Fischer, W. van der Wijngaart, G. Stemme, F. Niklaus, Flexible and Stretchable Microneedle Patches with Integrated Rigid Stainless Steel Microneedles for Transdermal Biointerfacing. *Plos One* **11** (12), e0166330 (2016).
32. F. Tehrani, H. Teymourian, B. Wuerstle, J. Kavner, R. Patel, A. Furnidge, R. Aghavali, H. Hosseini-Toudeshki, C. Brown, F. Y. Zhang, K. Mahato, Z. X. Li, A. Barfidokht, L. Yin, P. Warren, N. Huang, Z. Patel, P. P. Mercier, J. Wang, An integrated wearable microneedle array for the continuous monitoring of multiple biomarkers in interstitial fluid. *Nat. Biomed. Eng.*, 1-11 (2022).

33. S. D. Gittard, B. Chen, H. D. Xu, A. Ovsianikov, B. N. Chichkov, N. A. Monteiro-Riviere, R. J. Narayan, The effects of geometry on skin penetration and failure of polymer microneedles. *J. Adhes. Sci. Technol.* **27**, 227-243 (2013).
34. N. Arroyo-Curras, P. Dauphin-Ducharme, G. Ortega, K. L. Ploense, T. E. Kippin, K. W. Plaxco, Subsecond-Resolved Molecular Measurements in the Living Body Using Chronoamperometrically Interrogated Aptamer-Based Sensors. *ACS Sens.* **3**, 360-366 (2018).
35. Y. R. Xue, X. Li, H. B. Li, W. K. Zhang, Quantifying thiol-gold interactions towards the efficient strength control. *Nat. Commun.* **5**, 1-9 (2014).
36. R. T. Carvalhal, R. S. Freire, L. T. Kubota, Polycrystalline gold electrodes: A comparative study of pretreatment procedures used for cleaning and thiol self-assembly monolayer formation. *Electroanalysis* **17**, 1251-1259 (2005).
37. A. M. Downs, J. Gerson, M. N. Hossain, K. Ploense, M. Pham, H. B. Kraatz, T. Kippin, K. W. Plaxco, Nanoporous Gold for the Miniaturization of In Vivo Electrochemical Aptamer-Based Sensors. *ACS Sens.* **6**, 2299-2306 (2021).
38. N. Arroyo-Curras, K. Scida, K. L. Ploense, T. E. Kippin, K. W. Plaxco, High Surface Area Electrodes Generated via Electrochemical Roughening Improve the Signaling of Electrochemical Aptamer-Based Biosensors. *Anal. Chem.* **89**, 12185-12191 (2017).
39. P. Sondhi, K. J. Stine, "Electrodeposition of Nanoporous Gold Thin Films" in *Nanofibers-Synthesis, Properties and Applications*, B. Kumar, Ed. (IntechOpen, London, UK, 2020).
40. U. S. Mohanty, Electrodeposition: a versatile and inexpensive tool for the synthesis of nanoparticles, nanorods, nanowires, and nanoclusters of metals. *J. Appl. Electrochem.* **41**, 257-270 (2011).
41. Y. Xiao, R. Y. Lai, K. W. Plaxco, Preparation of electrode-immobilized, redox-modified oligonucleotides for electrochemical DNA and aptamer-based sensing. *Nat. Protoc.* **2**, 2875-2880 (2007).
42. H. Li, P. Dauphin-Ducharme, G. Ortega, K. W. Plaxco, Calibration-Free Electrochemical Biosensors Supporting Accurate Molecular Measurements Directly in Undiluted Whole Blood. *J. Am. Chem. Soc.* **139**, 11207-11213 (2017).
43. A. M. Downs, J. Gerson, K. L. Ploense, K. W. Plaxco, P. Dauphin-Ducharme, Subsecond-Resolved Molecular Measurements Using Electrochemical Phase Interrogation of Aptamer-Based Sensors. *Anal. Chem.* **92**, 14063-14068 (2020).
44. J. A. Nick, S. M. Moskowitz, J. F. Chmiel, A. V. Forssen, S. H. Kim, M. T. Saavedra, L. Saiman, J. L. Taylor-Cousar, D. P. Nichols, Azithromycin may antagonize inhaled tobramycin when targeting *Pseudomonas aeruginosa* in cystic fibrosis. *Ann. Am. Thorac. Soc.* **11**, 342-350 (2014).
45. G. M. Pacifici, K. Allegaert, Clinical pharmacokinetics of vancomycin in the neonate: a review. *Clinics* **67**, 831-837 (2012).
46. J. W. Xu, Y. T. Zhu, P. G. Niu, Y. Liu, D. Y. Li, L. Jiang, D. H. Shi, Establishment and application of population pharmacokinetics model of vancomycin in infants with meningitis. *Pediatr. Neonatol.* **63**, 57-65 (2022).
47. M. W. Konstan, M. D. Schluchter, W. Xue, P. B. Davis, Clinical use of ibuprofen is associated with slower FEV1 decline in children with cystic fibrosis. *Am. J. Respir. Crit. Care Med.* **176**, 1084-1089 (2007).

48. A. M. V. Mohan, J. R. Windmiller, R. K. Mishra, J. Wang, Continuous minimally-invasive alcohol monitoring using microneedle sensor arrays. *Biosens. Bioelectron.* **91**, 574-579 (2017).
49. J. W. Seo, K. Y. Fu, S. Correa, M. Eisenstein, E. A. Appel, H. T. Soh, Real-time monitoring of drug pharmacokinetics within tumor tissue in live animals. *Sci. Adv.* **8** (1), eabk2901 (2022).
50. R. Brogden, R. Pinder, P. R. Sawyer, T. Speight, G. Avery, Tobramycin: a review of its antibacterial and pharmacokinetic properties and therapeutic use. *Drugs* **12**, 166-200 (1976).
51. K. K. Leung, A. M. Downs, G. Ortega, M. Kurnik, K. W. Plaxco, Elucidating the Mechanisms Underlying the Signal Drift of Electrochemical Aptamer-Based Sensors in Whole Blood. *ACS Sens.* **6**, 3340-3347 (2021).
52. Z. Y. Wang, J. Y. Luan, A. Seth, L. Liu, M. L. You, P. Gupta, P. Rathi, Y. X. Wang, S. S. Cao, Q. S. Jiang, X. Zhang, R. Gupta, Q. J. Zhou, J. J. Morrissey, E. L. Scheller, J. S. Rudra, S. Singamaneni, Microneedle patch for the ultrasensitive quantification of protein biomarkers in interstitial fluid. *Nat. Biomed. Eng.* **5**, 64-76 (2021).
53. W. Martanto, J. S. Moore, T. Couse, M. R. Prausnitz, Mechanism of fluid infusion during microneedle insertion and retraction. *J. Controlled Release* **112**, 357-361 (2006).
54. C. Kolluru, M. Williams, J. S. Yeh, R. K. Noel, J. Knaack, M. R. Prausnitz, Monitoring drug pharmacokinetics and immunologic biomarkers in dermal interstitial fluid using a microneedle patch. *Biomed. Microdevices* **21**, 1-9 (2019).
55. P. A. Vieira, C. B. Shin, N. Arroyo-Curras, G. Ortega, W. W. Li, A. A. Keller, K. W. Plaxco, T. E. Kippin, Ultra-High-Precision, in-vivo Pharmacokinetic Measurements Highlight the Need for and a Route Toward More Highly Personalized Medicine. *Front Mol Biosci* **6**, 69 (2019).
56. L. Lin, L. Grenier, Y. Bergeron, M. Simard, M. G. Bergeron, G. Labrecque, D. Beauchamp, Temporal Changes of Pharmacokinetics, Nephrotoxicity, and Subcellular-Distribution of Tobramycin in Rats. *Antimicrob. Agents Chemother.* **38**, 54-60 (1994).
57. P. P. Samant, M. R. Prausnitz, Mechanisms of sampling interstitial fluid from skin using a microneedle patch. *Proc. Natl. Acad. Sci. U.S.A.* **115**, 4583-4588 (2018).
58. A. H. Bretag, Synthetic Interstitial Fluid for Isolated Mammalian Tissue. *Life Sci. Pt. 1 Physi.* **8**, 319-329 (1969).
59. N. Arroyo-Curras, G. Ortega, D. A. Copp, K. L. Ploense, Z. A. Plaxco, T. E. Kippin, J. P. Hespanha, K. W. Plaxco, High-Precision Control of Plasma Drug Levels Using Feedback-Controlled Dosing. *Acs Pharmacol. Transl.* **1**, 110-118 (2018).
60. Y. C. Zhao, B. Wang, H. Hojajji, Z. Q. Wang, S. Y. Lin, C. Yeung, H. S. Lin, P. Nguyen, K. L. Chiu, K. Salahi, X. B. Cheng, J. W. Tan, B. A. Cerrillos, S. Emaminejad, A wearable freestanding electrochemical sensing system. *Sci. Adv.* **6**, eaaz0007 (2020).
61. M. Mitra, H. N. Lee, H. A. Collier, Determining Genome-wide Transcript Decay Rates in Proliferating and Quiescent Human Fibroblasts. *J. Vis. Exp.* **131**, e56423 (2018).
62. W. Strober, Trypan blue exclusion test of cell viability. *Curr. Protoc. Immunol.* **21** (1), A-3B (1997).
63. S. Liang, Y. C. Han, W. L. H. Zhang, T. Y. Zhong, H. Y. Guan, Y. F. Song, Y. Zhang, L. L. Xing, X. Y. Xue, G. L. Li, Y. Zhan, A self-powered wearable body-detecting/brain-stimulating system for improving sports endurance performance. *Nano Energy* **93**, 106851 (2022).

64. L. Thorsteinn, *Essential pharmacokinetics : a primer for pharmaceutical scientists* (Elsevier/AP, Boston, MA, 2015).
65. G. Schmelzeisen-Redeker, M. Schoemaker, H. Kirchsteiger, G. Freckmann, L. Heinemann, L. Del Re, Time delay of CGM sensors: relevance, causes, and countermeasures. *J. Diabetes Sci. Technol.* **9**, 1006-1015 (2015).

Acknowledgments: The authors thank Dr. Matthew Savary, Dr. Russell B. Kerbel, and Dr. Matthew Davis for sharing expertise, and Yu Chen for assistance with setting up the standard molecular assays.

Funding:

National Science Foundation (Award 1847729, SE)
Brain and Behavior Foundation (National Alliance for Research on Schizophrenia & Depression Young Investigator Grant, SE)
Precise Advanced Technologies and Health Systems for Underserved Populations (PATHS-UP, NSF Engineering Research Center, Award 648451, SE)
Startup package provided by the UCLA Henry Samueli School of Engineering and Applied Sciences (SE)
NIH/NCI CA221296-01A1 (HC)
Melanoma Research Alliance (Grant ID 564714, HC)
UCLA Dissertation Year Fellowship (SL)
UCLA Graduate Dean's Scholar Award (JZ)

Author contributions:

Conceptualization: SL, XC, JZ, SE
Microneedle aptamer sensor fabrication and characterization: SL, XC, JZ, TW
Biocompatibility and microneedle insertion test: DJ, JZ, AH
In-vivo animal test: JZ, SL, TW
Blood analysis: XC
Data analysis and interpretation: SL, XC, JZ, BW, DJ, YZ, TW, AH, JT, JY, WY, SF, HC, CM, SE
Supervision: SE
Writing – original draft: SL, XC, JZ, SE
Writing – review & editing: SL, XC, JZ, BW, DJ, YZ, TW, AH, JT, JY, WY, SF, HC, CM, SE

Competing interests: SE, SL, JZ, XC are inventors on a provisional patent application (U.S. Prov App No. 63/317,019) related to some aspects of the presented technology. The other authors declare that they have no competing interests.

Data and materials availability: All data are available in the main text or the supplementary materials.

Figures

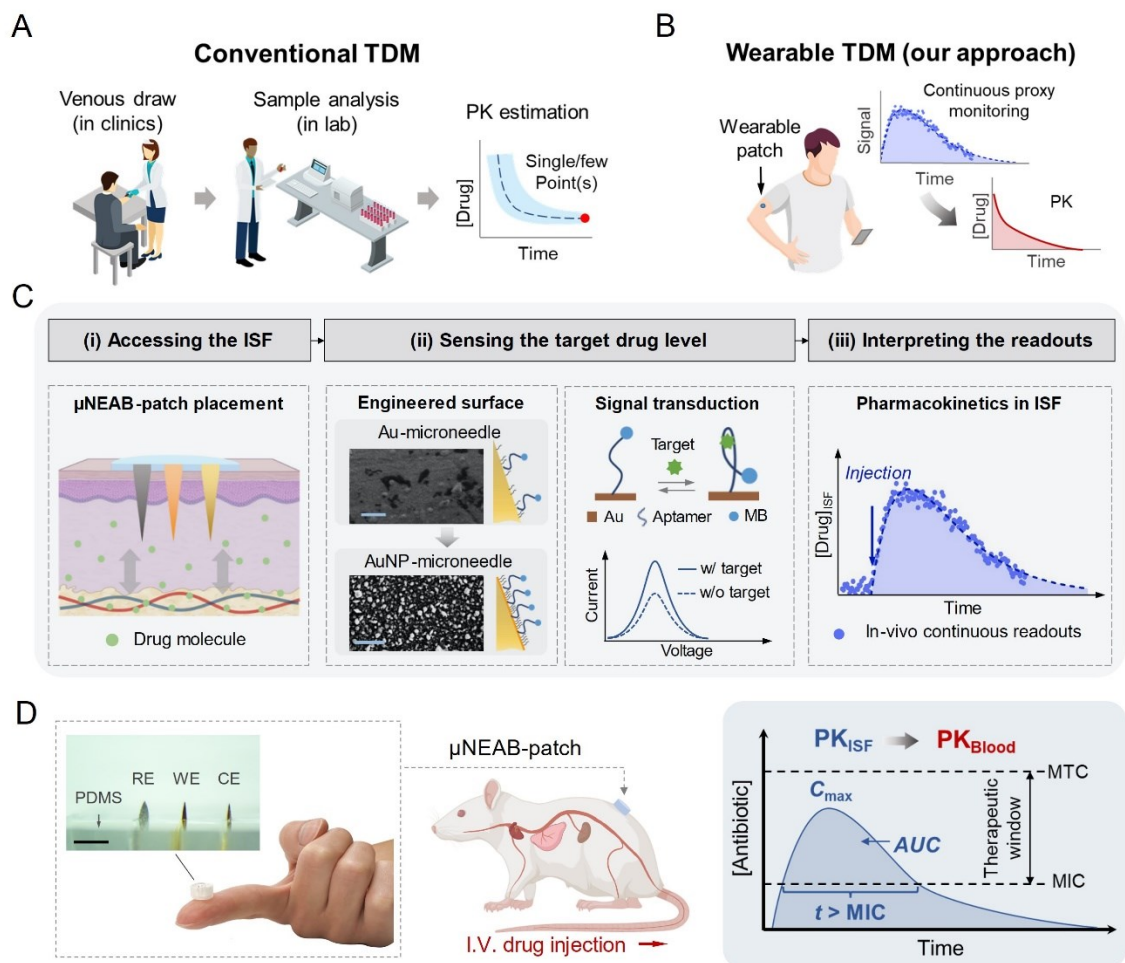


Fig. 1. μ NEAB-patch for wearable TDM. (A) Schematic illustration of the procedures involved in conventional TDM approaches. These approaches rely on venous blood draw in clinics followed by analysis in a centralized lab and render limited measurement(s) of the drug's circulating level to estimate the drug's PK. (B) Schematic illustration of the envisioned wearable TDM modality. A wearable patch tracks the drug level in ISF continuously and in real-time to infer the drug's PK. (C) Wearable TDM enabled by the μ NEAB-patch: (i) The drug molecules in the dermal ISF are minimally-invasively accessed by the patch. (ii) The engineered AuNP-microneedle substrate renders reliable aptamer immobilization and efficient transduction of the target-aptamer binding events into voltammetric readouts. Insets show the SEM images of bare and AuNP-microneedle electrode surfaces (scale bars: 5 μ m). (iii) In-vivo continuous readouts are used to infer the drug's PK. (D) Left: photos of an assembled μ NEAB-patch, consisting of microneedle electrodes embedded in an elastomeric substrate (PDMS). WE, CE, and RE correspondingly denote working, counter, and reference electrodes. Scale bar: 2 mm. Middle: schematic representation of a μ NEAB-patch applied in a rat model for in-vivo TDM. Right: Utility of the μ NEAB-patch for inferring the pharmacokinetic characteristics of antibiotics. MTC and MIC denote minimally toxic and inhibitory concentrations, respectively.

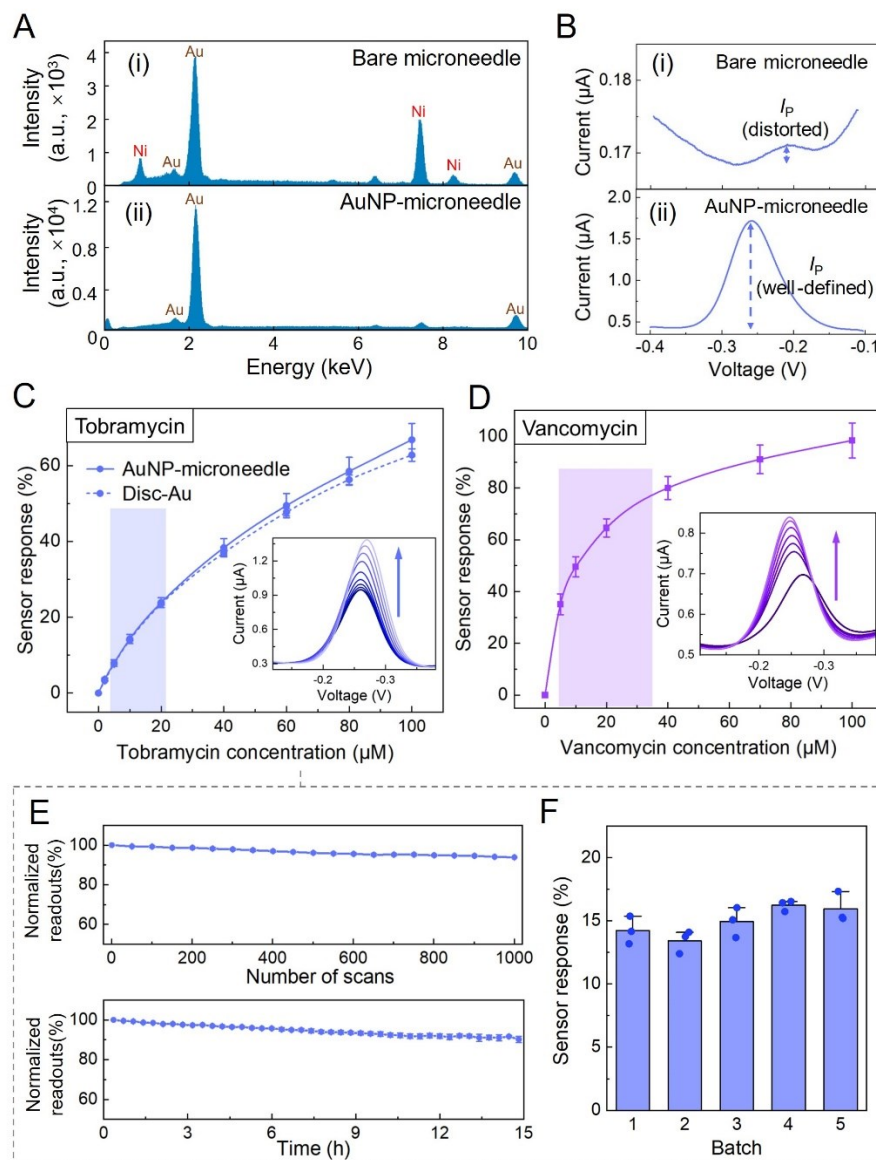


Fig. 2. Development and characterization of μNEABs . (A) EDS spectrum of a bare microneedle surface (i) and an AuNP-microneedle surface (ii). (B) Square wave voltammograms of μNEABs constructed on bare microneedle (i) and AuNP-microneedle (ii) substrates. (C) Response of tobramycin μNEABs , in comparison with tobramycin EABs constructed on gold disc electrodes. Error bars indicate standard deviations ($n = 5$). Inset shows the square wave voltammograms acquired from a μNEAB with 0, 2, 5, 10, 20, 40, 60, 80, 100 μM tobramycin (arrow indicates the increase of concentration). (D) Response of vancomycin μNEABs . Error bars indicate standard deviations ($n = 5$). Inset shows the corresponding square wave voltammograms with 0, 5, 10, 20, 40, 70, 100 μM vancomycin (arrow indicates the increase of concentration). The shaded area in (C,D) indicates the target therapeutic window for the respective drug. (E) Normalized tobramycin μNEAB readout variations under repetitive interrogation (upper panel) and with extended operation time (lower panel). Error bars indicate standard deviations ($n = 3$). (F) Tobramycin μNEABs ' response to 10 μM tobramycin. Three sensors were characterized for

each batch. Error bars indicate standard deviations. All the experiments were performed in artificial ISF buffer solutions.

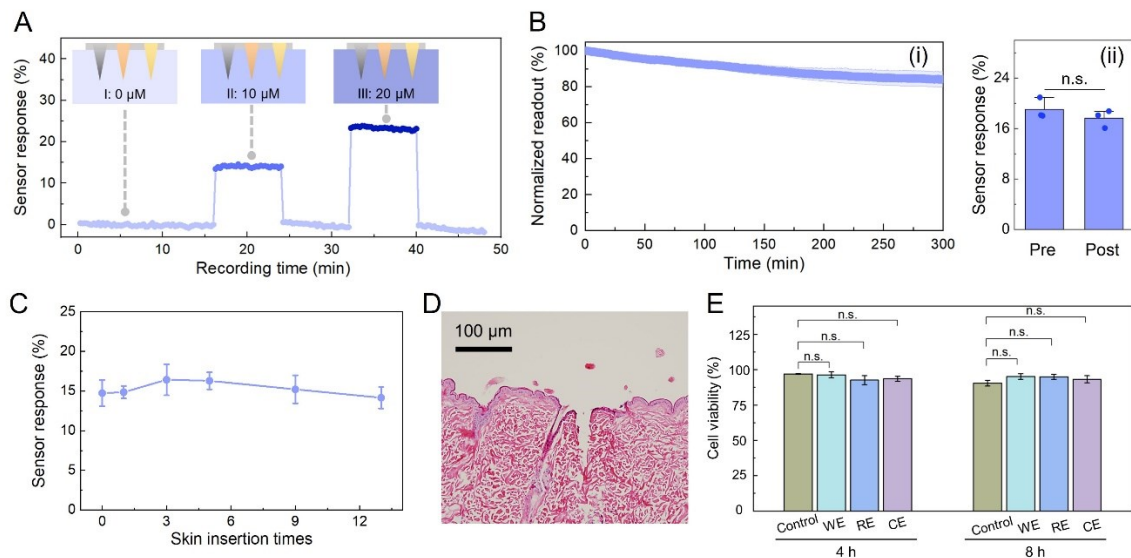


Fig. 3. Ex-vivo μ NEAB-patch characterization. (A) Continuous measurements of μ NEAB-patch sensing response in a phantom gel setup. The μ NEAB-patch was inserted into three phantom gels in a rotational manner. Inserts show the schematics of the testing setup. Tobramycin concentration levels in the three testing gels: 0, 10, and 20 μ M. (B) (i) Normalized continuous μ NEAB readouts in a hydrated rat skin tissue. (ii) Comparison of the μ NEABs' response to 10 μ M tobramycin before and \sim 300 min after skin tissue exposure. The error band/bars in (i)/(ii) indicate the standard deviations ($n = 3$). (C) μ NEAB responses to 10 μ M tobramycin before and after repetitive insertion into a porcine skin tissue. The error bars indicate the standard deviation ($n = 4$). (D) Photo of H&E-stained rat skin showing the penetration of a devised microneedle electrode. (E) Viability of HDFs cultured with medium exposed to μ NEAB electrodes for 4 and 8 hours. The control result refers to the test performed using a blank matrix. The error bars indicate the standard deviation of two biological and two technical replicates. 'n.s.' denotes statistical non-significance.

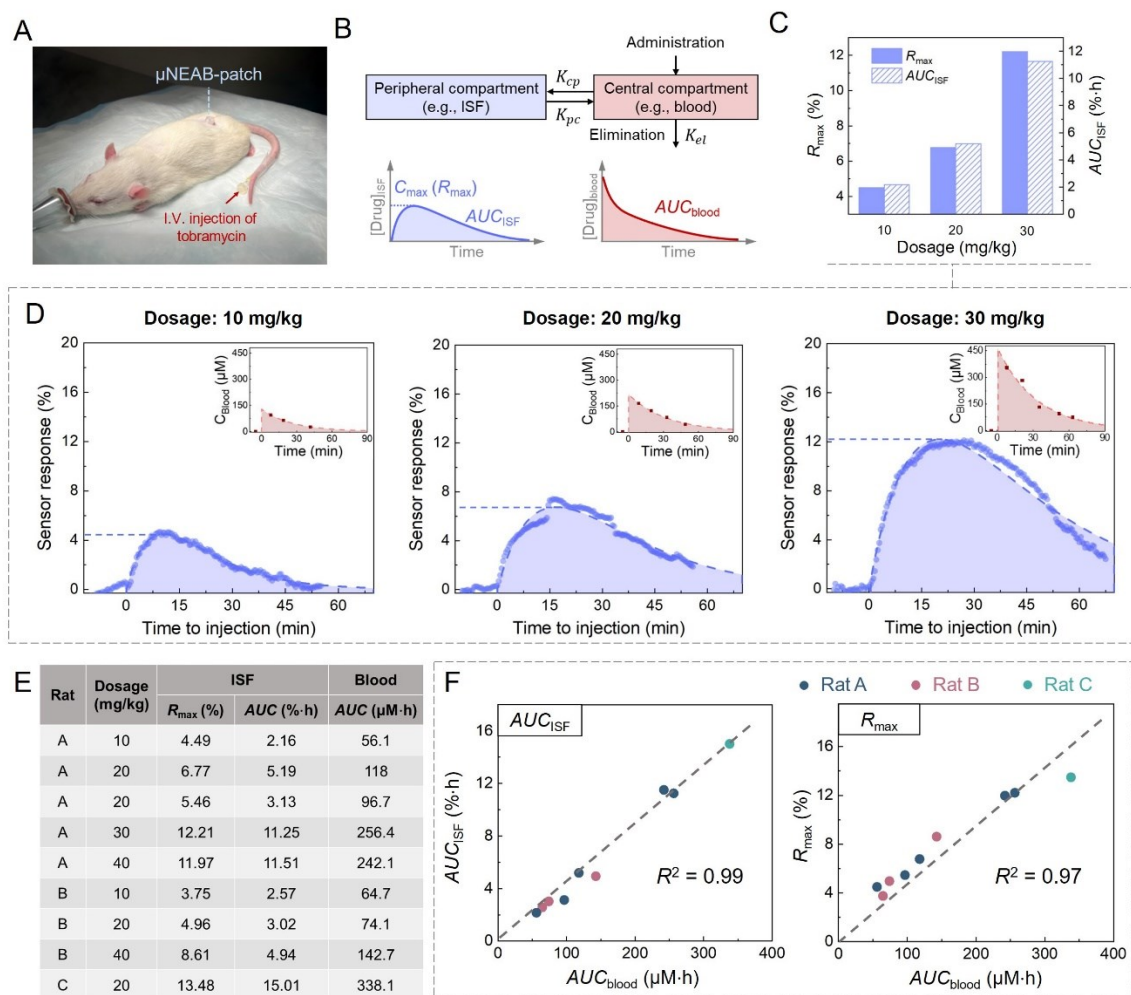


Fig. 4. In-vivo ISF correlation studies enabled by the μNEAB -patch. (A) Photo of the animal study setup. The μNEAB -patch was applied at the back of the rat and the drug was injected intravenously from the tail vein with the aid of a catheter. (B) Schematics of a two-compartment pharmacokinetic model and representative pharmacokinetic profiles in central and peripheral compartments. K_{pc} , K_{cp} , and K_{el} denote the first-order rate constants for distribution, redistribution, and elimination, respectively. (C) ISF PK parameters of one animal (rat A) with three different tobramycin doses. (D) The measured and baseline-corrected μNEAB -patch readouts of Figure 4C. Insets show the corresponding blood measurements. Dash lines show the fitted pharmacokinetic curves. (E) Tabulated PK results among three animals (nine trials). (F) Correlations between PK parameters in ISF and blood. Left: AUC_{blood} versus AUC_{ISF} ; right: AUC_{blood} versus R_{max} .

List of supplementary figures and tables

Fig. S1. Schematic of the μ NEAB-patch fabrication/assembly process for dermal application.

Fig. S2. Characterization of the μ NEAB-patch's mechanical properties.

Fig. S3. The response of AuNP-microneedle and bare microneedle electrodes to freely-diffusing MB.

Fig. S4. Illustration of the surface area enhancement effect using an AuNP coating.

Fig. S5. Calibration of μ NEABs.

Fig. S6. Validation of the μ NEABs' electrochemical readouts.

Fig. S7. Characterization of the μ NEAB's response time, reversibility, and selectivity.

Fig. S8. Characterization of the tobramycin μ NEAB's drift.

Fig. S9. Degradation of an Au-evaporated microneedle EAB.

Fig. S10. Demonstration of the μ NEAB's minimally-invasiveness.

Fig. S11. Characterization of the μ NEAB's biocompatibility.

Fig. S12. In-vivo biomonitoring using tobramycin μ NEAB-patches.

Fig. S13. In-vivo biomonitoring using a vancomycin μ NEAB-patch.

Fig. S14. Raw ISF PK monitoring results of one rat.

Fig. S15. Raw PK monitoring results of rat B.

Fig. S16. Extended analysis of in-vivo tobramycin PK monitoring results.

Supplementary Materials:

Wearable microneedle-based electrochemical aptamer biosensing for personalized dosing of drugs with narrow therapeutic windows

Shuyu Lin^{1,2,†}, Xuanbing Cheng^{1,2,3,†}, Jialun Zhu^{1,2,3,†}, Bo Wang^{1,2}, David Jelinek^{4,5}, Yichao Zhao^{1,2,3}, Tsung-Yu Wu^{1,2,3}, Abraham Horrillo⁴, Jiawei Tan^{1,2,3}, Justin Yeung^{1,3}, Wenzhong Yan⁷, Sarah Forman^{1,4}, Hilary A. Collier^{4,6,8}, Carlos Milla⁹, Sam Emaminejad^{1,2,10*}

Affiliations

¹Interconnected & Integrated Bioelectronics Lab (I²BL), University of California, Los Angeles.

²Department of Electrical and Computer Engineering, University of California, Los Angeles.

³Department of Materials Science and Engineering, University of California, Los Angeles.

⁴Department of Molecular, Cell and Developmental Biology, University of California, Los Angeles.

⁵Weintraub Center for Reconstructive Biotechnology, School of Dentistry, University of California, Los Angeles.

⁶Department of Biological Chemistry, David Geffen School of Medicine, University of California, Los Angeles.

⁷Department of Mechanical and Aerospace Engineering, University of California, Los Angeles.

⁸Molecular Biology Institute, University of California, Los Angeles.

⁹The Stanford Cystic Fibrosis Center, Center for Excellence in Pulmonary Biology, Stanford School of Medicine.

¹⁰Department of Bioengineering, University of California, Los Angeles.

†These authors contributed equally to this work.

*Correspondence and requests for materials should be addressed to S.E. (emaminejad@ucla.edu)

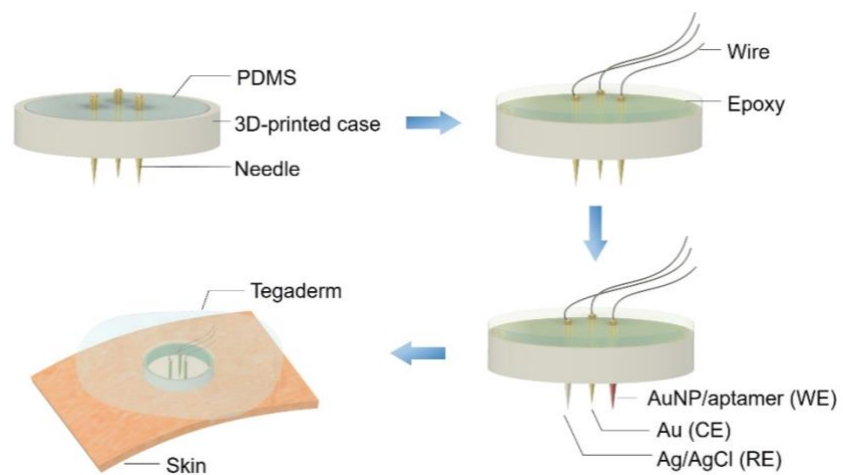


Fig. S1. Schematic of the μ NEAB-patch fabrication/assembly process for dermal application.

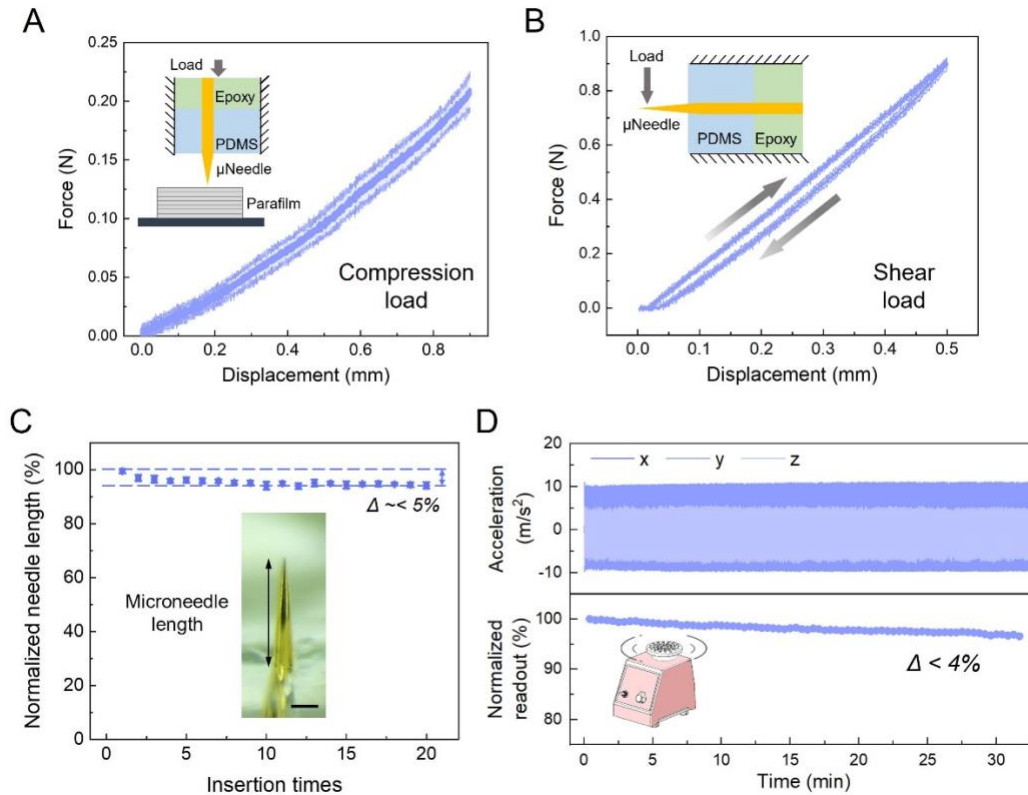


Fig. S2. Characterization of the μ NEAB-patch's mechanical properties. (A, B) Force vs. displacement curves of a μ NEAB electrode under compression load (A) and shear load (B). A single-electrode microneedle device (bare microneedle) was used for these tests. The error bands indicate standard deviations ($n = 3$). Insets show the characterization setup. For both cases, the smooth curves indicate that no microneedle crack was formed during compression/shearing. The compression study indicates an equivalent insertion force of about 0.2 N is required to achieve a displacement of 1 mm (corresponding to the length of the microneedle). The negligible net displacement observed at the end of the loading cycle in the shear force study indicates the preservation of the device's structural integrity. (C) Characterization of the length of a single microneedle electrode after repetitive porcine skin insertion, indicating minimal variation ($\sim 5\%$). Error bars indicate standard deviations ($n = 3$). Inset shows the optical image of one microneedle electrode after 20 insertions with no observable needle deformation (bending, cracking, *etc.*). Scale bar indicates 200 μ m. (D) Normalized tobramycin μ NEAB-patch's continuous readout in porcine skin under 3D oscillatory acceleration conditions (rendered by a vortex mixer). The corresponding patch readouts and vibrational acceleration profiles are presented in the bottom and top panels, respectively. The sensor readout exhibits negligible fluctuations ($< 4\%$), despite the induced motion.

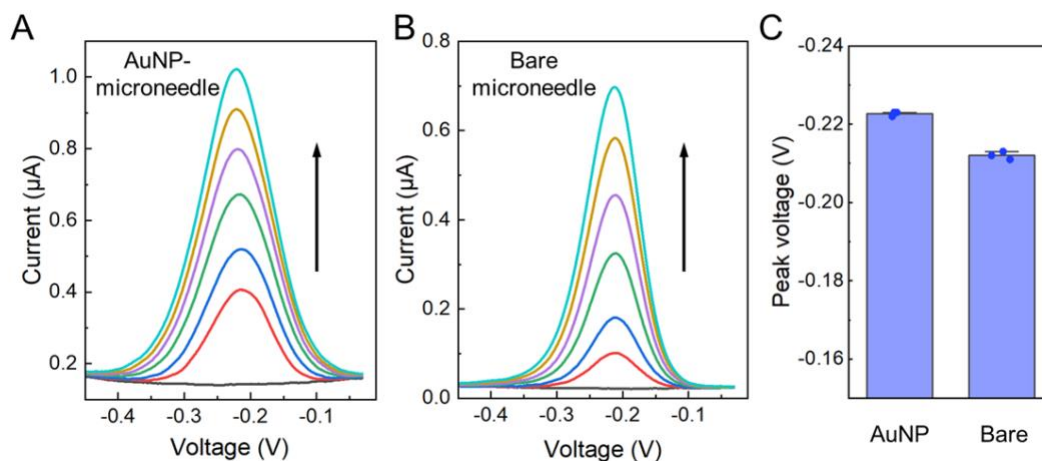


Fig. S3. The response of AuNP-microneedle and bare microneedle electrodes to freely-diffusing MB. (A, B) Square wave voltammograms of AuNP-microneedle (A) and bare microneedle (B) electrodes to 0, 10, 20, 40, 60, 80, 100 μM MB in artificial ISF solutions. Arrows indicate the increase of concentration. (C) Comparison of MB's peak voltage as measured by the two electrodes ($n = 3$). The microneedle electrodes were coated with 6-mercapto-1-hexanol only, following a similar fabrication process as μNEABs (without involving aptamer immobilization). Both electrodes demonstrate well-defined voltammetric response to freely-diffusing methylene blue with a similar peak potential position as measurements in Fig. 2B. The results suggest that the change of the electrode surface does not significantly alter the MB's electrochemical activity.

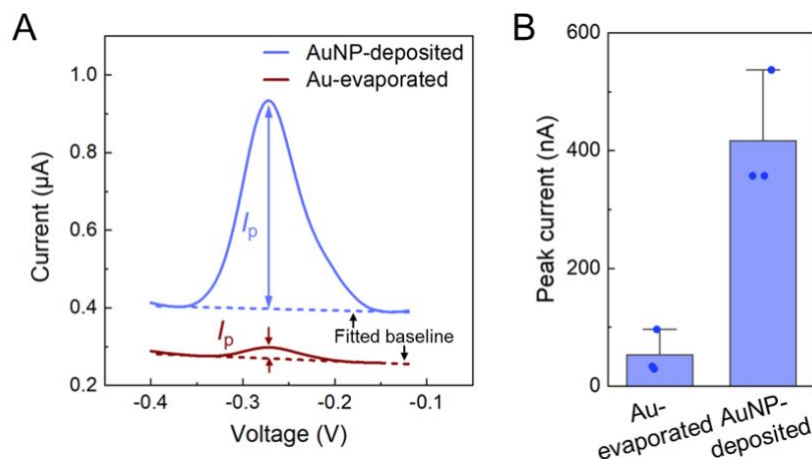


Fig. S4. Illustration of the surface area enhancement effect using an AuNP coating. (A) Square wave voltammograms of tobramycin μ NEABs constructed on AuNP-deposited and Au- evaporated microneedles (performed in artificial ISF solution). Annotations illustrate the adopted method for extracting the voltammetric current peak height (I_p), which serves as the sensor readout. (B) Corresponding AuNP- deposited and Au- evaporated μ NEABs' readouts. Error bars indicate standard deviations ($n = 3$).

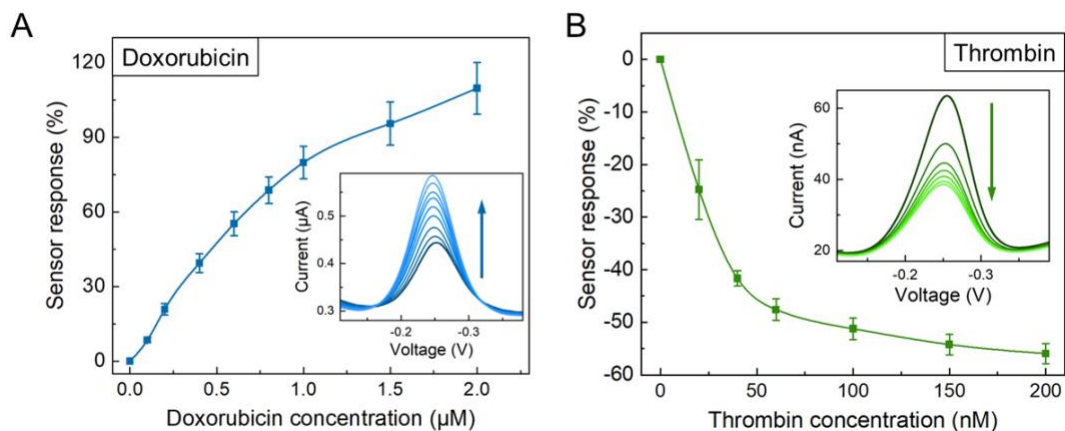


Fig. S5. Calibration of μ NEABs. Response of doxorubicin μ NEABs (**A**) and thrombin μ NEABs (**B**). Error bars indicate standard deviations ($n = 5$). Insets show the corresponding square wave voltammograms acquired from representative biosensors. Doxorubicin: 0, 0.1, 0.2, 0.4, 0.6, 1.0, 1.5, 2 μ M. Thrombin: 0, 20, 40, 60, 100, 100, 150, 200 nM. Arrows indicate the increase of concentration. The signal-off response of the thrombin μ NEABs (opposite to the other introduced μ NEABs) originate from the formation of G-quadruplex structure upon thrombin-aptamer binding, which causes the MB moiety (on the surface-bound aptamer) to be positioned further away from the sensor surface in the new structural state.

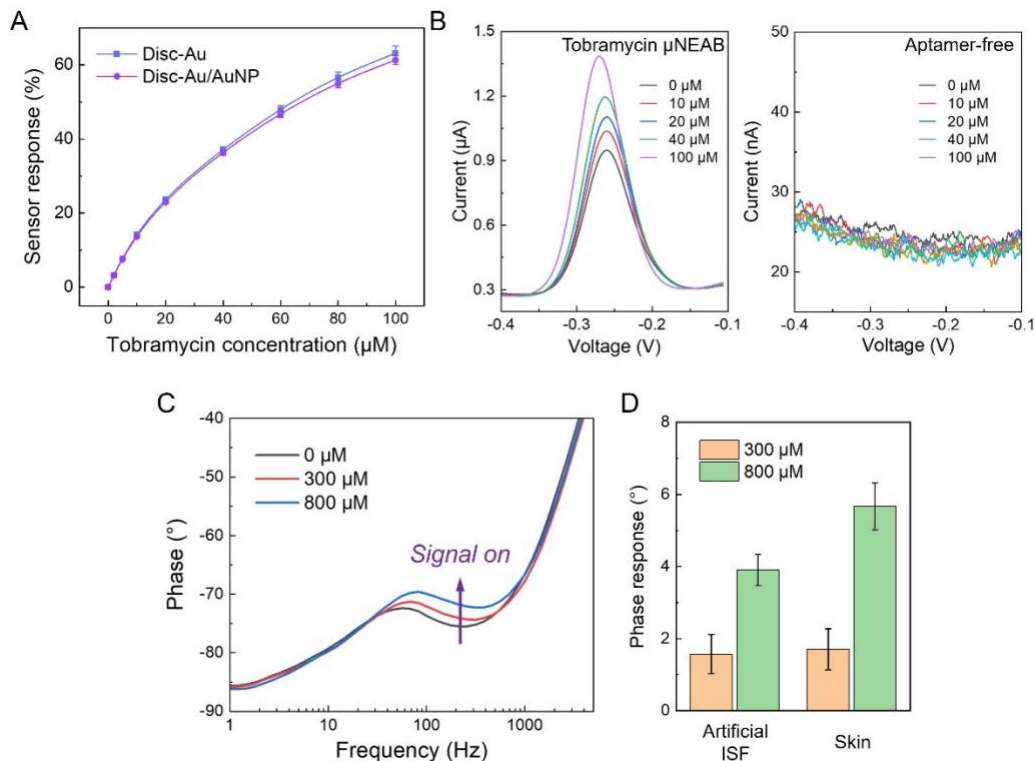


Fig. S6. Validation of the μ NEABs' electrochemical readouts. (A) Influence of AuNP coating on EABs on a standard gold electrode. Response of AuNP-coated vs. uncoated disc gold electrode. Error bars indicate standard deviations ($n = 3$). While capable of increasing the signal current level, the observed minimal difference in sensor response indicates that the AuNP coating does not change the sensitivity of EABs. (B) Comparison of the readouts of a tobramycin μ NEAB (from Fig. 2C) vs. a control aptamer-free device for different introduced tobramycin concentrations. The aptamer-free device does not present noticeable voltammetric peak or sensor response. (C) Impedance phase spectroscopies of a tobramycin μ NEAB immersed in artificial ISF solutions containing different tobramycin concentrations. The addition of target molecules causes the local peak of the electrochemical phase (which is correlated to the Faradic response of MB) to shift to higher frequencies, indicating an increased electron transfer rate between MB and the electrode. (D) Corresponding increased phase responses (with respect to blank readout; performed at ~ 200 Hz) of tobramycin μ NEABs that were tested in artificial ISF solutions and pre-soaked porcine skin samples. The captured measurement in the two settings show a similar trend. Three μ NEABs were tested for each condition and error bars indicate standard deviations.

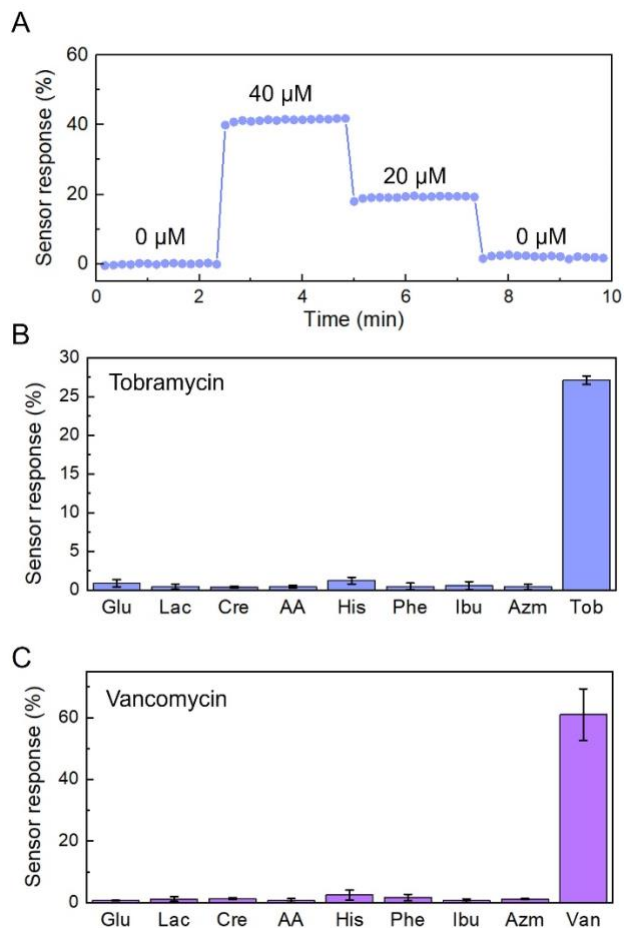


Fig. S7. Characterization of the μ NEAB's response time, reversibility, and selectivity. (A) Tobramycin μ NEAB response in artificial ISF solutions containing different tobramycin concentrations, demonstrating a rapid and reversible response (recording was paused during solution exchange; < 0.5 min). (B, C) Selectivity study of tobramycin (B) and vancomycin (C) μ NEABs. The tests were performed in an electrochemical cell. Error bars indicate standard deviations ($n = 3$). Concentration of interfering and target molecules: 5 mM glucose (Glu), 1 mM lactate (Lac), 80 μ M creatinine (Cre), 50 μ M ascorbic acid (AA), 100 μ M histidine (His), 200 μ M phenylalanine (Phe), 10 μ M ibuprofen (Ibu), 10 μ M azithromycin (Azm), 20 μ M tobramycin (Tob), 20 μ M vancomycin (Van).

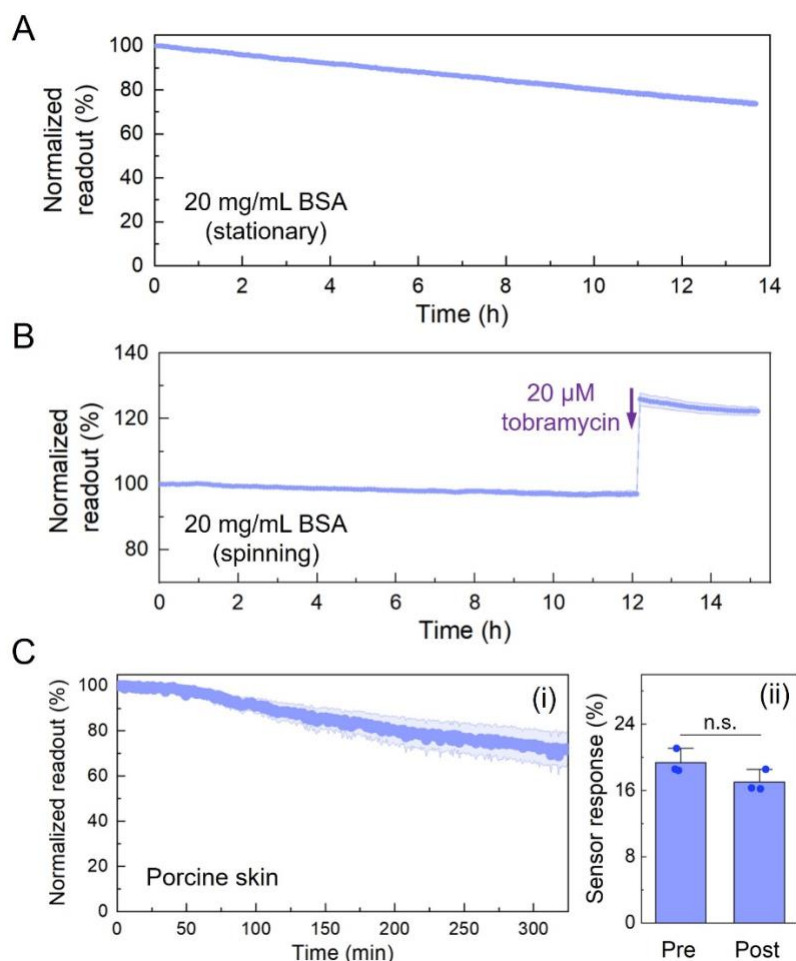


Fig. S8. Characterization of the tobramycin μ NEAB's drift. (A, B) Normalized continuous tobramycin μ NEAB readouts obtained in an artificial ISF solution containing 20 mg/mL BSA under stationary (A) and advective flow (B) conditions. Both tests were initiated in the absence of tobramycin. In (B), the advection was induced by a magnetic stirrer (radial frequency: 500 rpm) and the test solution was spiked with tobramycin at $t \sim 12$ h to reach a final concentration of 20 μ M. Error bands indicate standard deviations ($n = 3$). The observed lower drift rate in (B) as compared to (A) may be attributed to the perturbing effect of the fluid flow on the surface adhesion of the fouling agents (*e.g.*, large molecules such as proteins). (C) (i) Normalized continuous tobramycin μ NEAB readouts in a hydrated porcine skin tissue. (ii) Comparison of the μ NEABs' response to 10 μ M tobramycin before and ~ 300 min after skin tissue exposure. The error band/bars in (i)/(ii) indicate the standard deviations ($n = 4$) and n.s. denotes statistical non-significance ($p = 0.24$).

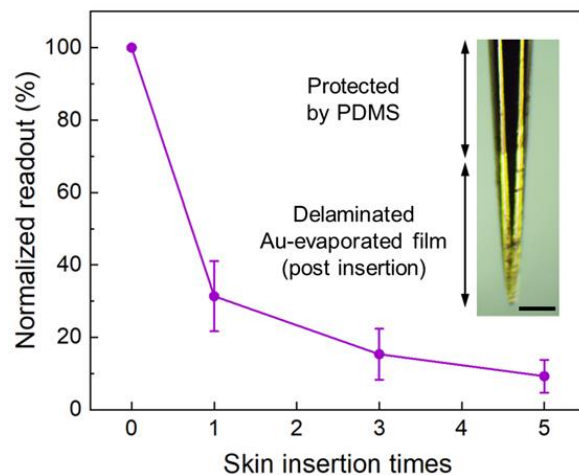


Fig. S9. Degradation of an Au-evaporated microneedle EAB. Normalized sensor readouts before and after repetitive insertions into a porcine skin tissue. The error bars indicate the standard deviations ($n = 3$). Inset shows the optical image of the device after five insertions, indicating the near-complete delamination of the Au-evaporated film from the substrate. Scale bar indicates 200 μm .

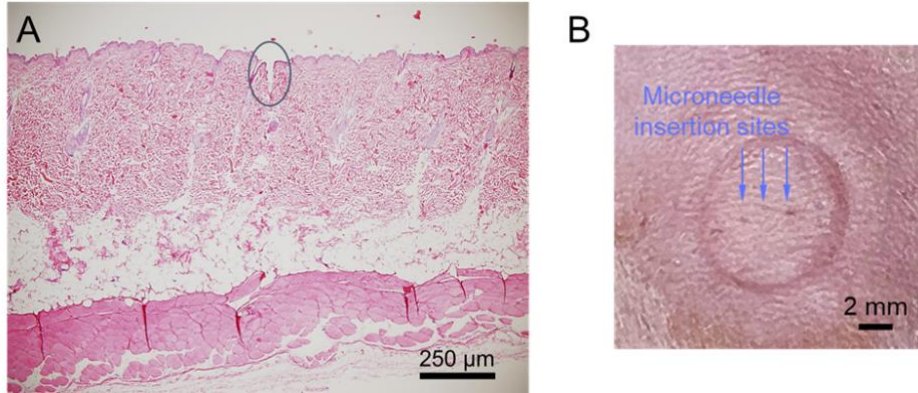


Fig. S10. Demonstration of the μ NEAB's minimally-invasiveness. (A) Zoom out view of the H&E-stained rat skin showing the microneedle insertion depth with respect to the whole skin structure. (B) Optical image of the rat skin immediately after the μ NEAB-patch removal. The insertion sites of the microneedle electrodes are annotated.

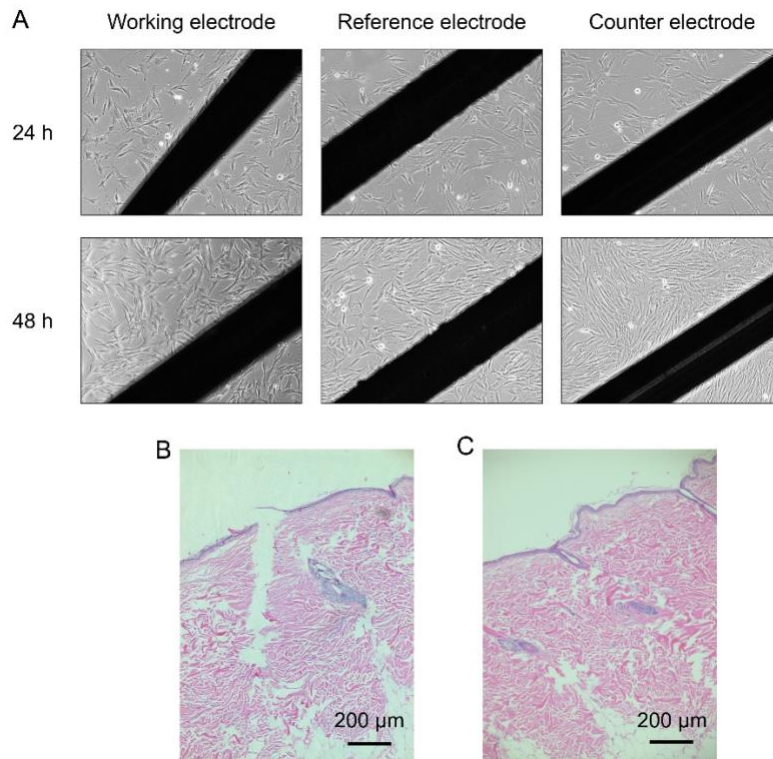


Fig. S11. Characterization of the μ NEAB's biocompatibility. (A) Representative optical images of HDFs in presence of three microneedle electrodes. The images were acquired 24 and 48 h post culturing. This experiment was performed in duplicates. (B,C) Representative H&E-stained rat skin at the microneedle insertion point (B) and a control site (no microneedle insertion, C). The H&E staining shows no observable morphological abnormality (*e.g.*, swelling or increased number of immune cells). This experiment was performed in duplicate, and no adverse reaction was observed in either animal.

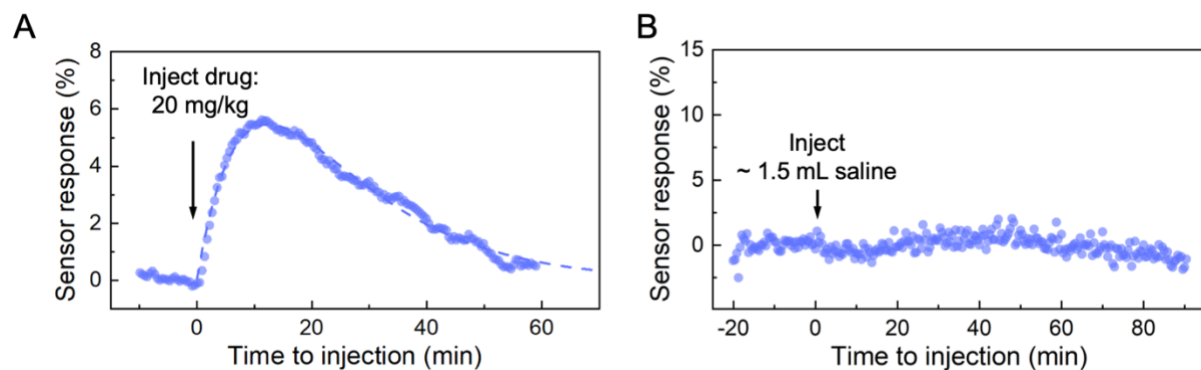


Fig. S12. *In-vivo* biomonitoring using tobramycin μ NEAB-patches. (A) Measured and baseline-corrected tobramycin μ NEAB-patch response to the tobramycin injection (injection dosage: 20 mg/kg). (B) Baseline-corrected tobramycin μ NEAB-patch response to the saline injection (serving as a vehicle control experiment).

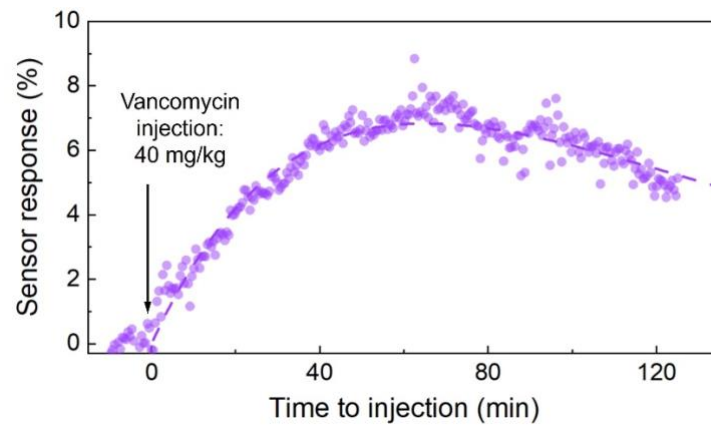


Fig. S13. *In-vivo* biomonitoring using a vancomycin μ NEAB-patch. Measured and baseline-corrected vancomycin μ NEAB-patch response to the vancomycin injection (injection dosage: 40 mg/kg; observation time window: 2 h).

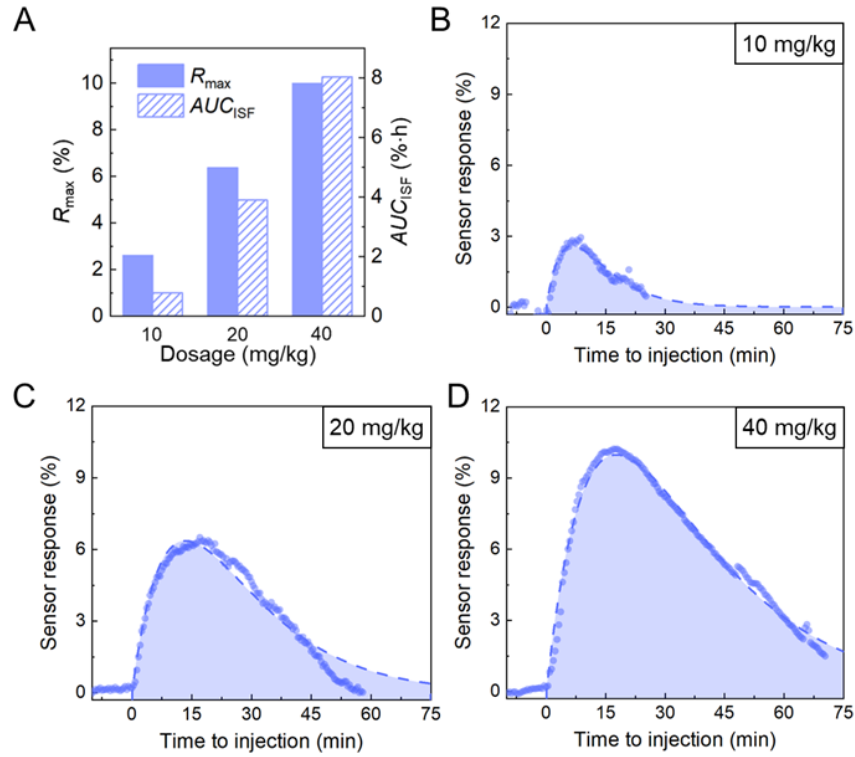


Fig. S14. Raw ISF PK monitoring results of one rat. (A) ISF PK parameters of one rat corresponding to three different tobramycin doses. (B-D) The measured and baseline-corrected μ NEAB-patch responses corresponding to the cases shown in (A). Dotted lines show the fitted pharmacokinetic curves.

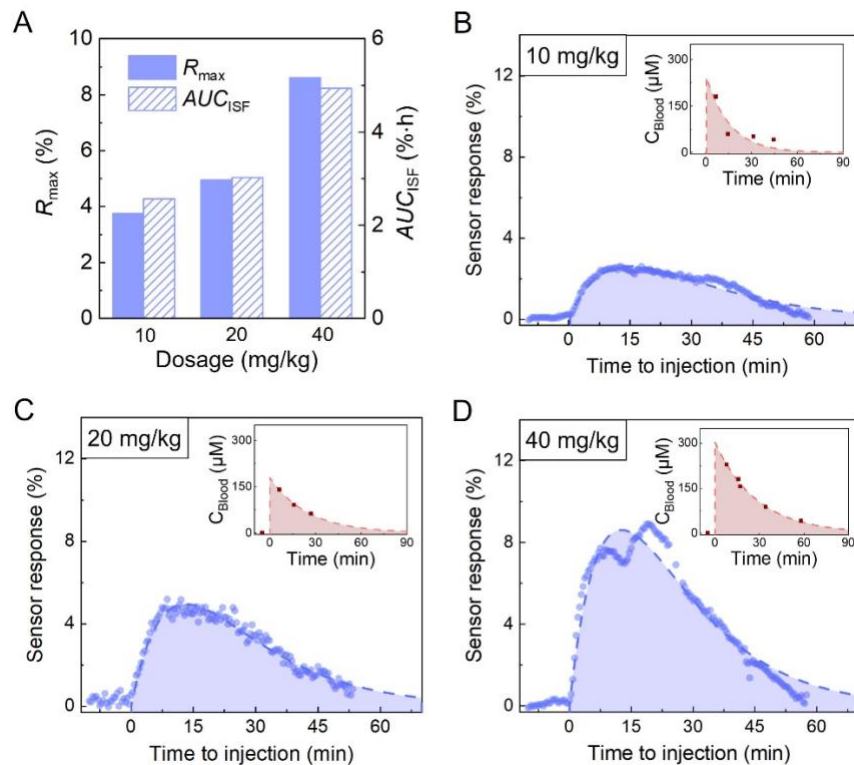


Fig. S15. Raw PK monitoring results of rat B. (A) ISF PK parameters of rat B corresponding to three different tobramycin doses. (B-D) The measured and baseline-corrected μNEAB -patch responses corresponding to the cases shown in (A). Insets show the corresponding blood measurements. Dotted lines show the fitted pharmacokinetic curves.

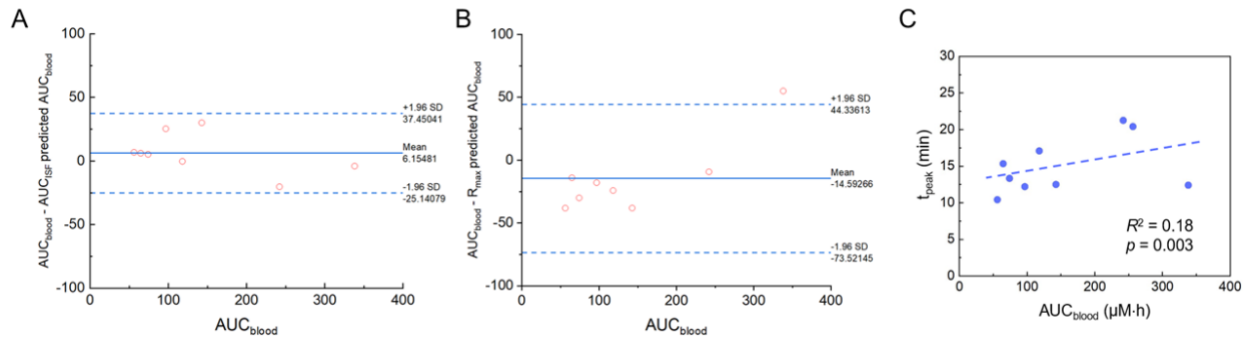


Fig. S16. Extended analysis of *in-vivo* tobramycin PK monitoring results. (A, B) Bland-Altman plots comparing the measured AUC_{blood} with the AUC_{ISF} -predicted (A) and the R_{max} -predicted (B) values. (C) Time-to-peak values (t_{peak}) of ISF readings upon injection. Comparison with AUC_{blood} illustrates a relatively weak correlation between t_{peak} and the total drug exposure ($R^2 = 0.18$, $p = 0.003$).

Table S1. Material cost of a fabricated μ NEAB-patch.

	Component	Cost (USD)
Device constituents	Needles	0.15
	PDMS	0.08
	3D-printed case	0.01
	AuNP	0.05
	Total	0.29
Sensing layers	Aptamer	2
	MCH	0.02
	Total	2.02
	Total	2.31